Towards Optimal Capacity-Achieving Transceivers with Photonic Integrated Circuits

by

Mihika Prabhu

Submitted to the Department of Electrical Engineering and Computer Science
in partial fulfillment of the requirements for the degree of

Master of Science in Electrical Engineering and Computer Science

at the

MASSACHUSETTS INSTITUTE OF TECHNOLOGY

February 2018

Signature redacted

Author .....
Department of Electrical Engineering and Computer Science
January 31, 2018

Signature redacted

Certified by .....
Dirk R. Englund
Associate Professor of Electrical Engineering and Computer Science
Thesis Supervisor

Signature redacted

Accepted by .....
Leslie A. Kolodziejski
Professor of Electrical Engineering and Computer Science
Chair, Department Committee on Graduate Students

Towards Optimal Capacity-Achieving Transceivers with Photonic Integrated Circuits

by

Mihika Prabhu

Submitted to the Department of Electrical Engineering and Computer Science
on January 31, 2018, in partial fulfillment of the
requirements for the degree of
Master of Science in Electrical Engineering and Computer Science

Abstract

Optical communication systems have many advantages over communication systems that operate in the radio-frequency range, including decreased size, weight, and power consumption and increased bandwidth. As a result, optical communication systems are emerging as the ideal choice in many resource-constrained links such as those deployed on spacecraft. This thesis presents progress on development of a programmable nanophotonic processor (PNP) for implementing a high-fidelity reconfigurable optical transceiver at the telecommunications wavelength. By encoding information in multiple spatial modes and detecting jointly over the modes using a unitary transform prior to detection, one can in principle attain Holevo-limited channel capacity in the low mean photon number regime. Since the PNP offers dynamic reprogrammability, one can also, in principle, correct for wavefront distortion in the channel. We present a setup, calibration protocols, and preliminary results towards a turbulence-resistant integrated BPSK transmitter and joint detection receiver channel that achieves superadditive channel capacity in the low mean photon number regime.

Thesis Supervisor: Dirk R. Englund
Title: Associate Professor of Electrical Engineering and Computer Science

Acknowledgments

I have had the immense fortune of being surrounded by an amazing network of mentors, peers, family, and friends, without whom this work would not have been possible. I would first like to thank my advisor, Professor Dirk Englund, for his guidance throughout the years and for introducing me to the field of nanophotonics. His availability to provide feedback, even at a moment's notice, has been an invaluable resource during this project and others. I would also like to give special thanks to Dr. Nick Harris for his mentorship, friendship, and enthusiastic support, no matter what the problem may be. I would additionally like to extend my thanks to Professor Saikat Guha for valuable discussions about the project and possible future directions and my funding source, the National Science Foundation, for supporting this project.

Late nights and weekends at the lab were brought to life by the camaraderie of my colleagues and friends in the Quantum Photonics Group. In particular, I would like to thank Darius Bunandar, Dr. Jacques Carolan, Ben Lienhard, Cheng Peng, Chris Panuski, Michael Walsh, Jiabao Zheng, Eric Bersin, Erik Eisenach, and Greg Steinbrecher. I have learned so much from our discussions and am grateful to have a group of friends who inspire each other to be the best scientists and human beings we can be. Thanks, everyone!

Last but not least, I am eternally grateful to my parents, Rajini Prabhu and Dr. Nagabhushana Prabhu, and to my brother, Ani Prabhu. Thank you for the unconditional love, support, and roasting. I would not be where I am today without you.

Contents

List of Figures

List of Tables

Chapter 1

Introduction

Exploration of the frontiers of space hinges on high-speed communication between spacecraft and the earth, navigating accurately, and remotely sensing the environment. Optical communication systems offer significant enhancements over radio frequency (RF) communication in terms of system mass, power consumption, precision tracking, flexibility in terms of government regulation, and data rate [4]. However, to keep up with the demands of a space communication network consisting of a large number of earth- and space-based nodes, we need to develop communication systems with improved security, bandwidth, and reliability, while also reducing size, weight, and power (SWaP). Integrated photonics is a very promising framework for developing such systems. In recent years, many reliable foundries have been created worldwide in response to the growing demand for photonics in industry and academia [5]. This thesis presents developments towards an integrated silicon-photonics platform called the programmable nanophotonic processor (PNP). The target application presented is an optical transceiver that promises high data-rate, quantum-enhanced optical communication over inter-satellite links (ISLs) and earth-satellite links (ESLs) while maintaining low size, weight, and power (SWaP) and being resistant to phase front distortion from atmospheric turbulence.

The following sections in this chapter contain background on the architecture of the reconfigurable photonic integrated chip (PIC) for arbitrary unitary transformations, basic communication channel structure and metrics, and description of a

recently proposed interferometric receiver architecture for high-capacity communications. Chapter two describes the setup of the PIC, along with engineering considerations regarding optical coupling, electrical control, and thermal stability. Chapter three describes methods for precise characterization and control of the active elements on the chip. Chapter four contains the design of an integrated photonic transceiver chip and channel, along with preliminary data towards its performance. Chapter five discusses future directions and avenues that will be explored to increase the performance of some or all of the components of the channel.

1.1 Programmable Nanophotonic Processor (PNP)

The basic building block of the PNP is the Mach-Zehnder interferometer (MZI), which performs the function of a variable-ratio beamsplitter between two input waveguide modes [6]. The architecture of the PNP is a tiled mesh consisting of 11 layers of 2x2 MZIs fabricated in the silicon-on-insulator process using the OpSIS foundry [7]. Knowing the transfer matrix of a single MZI, we can construct a model that simulates the transform applied by the PNP with a certain set of predefined phase settings to a user-defined input light vector.

MZIs

An ideal MZI can be divided into four stages: an input 50:50 directional coupler, an internal phase shifter θ, another 50:50 directional coupler, and an external phase shifter ϕ. Given the matrix transforms of each of the four stages separately, the transform of the entire MZI is simply a cascade of these four stages, represented by the following matrix product:

$$T = \begin{bmatrix} e^{i\phi(\vec{v})} & 0 \\ 0 & 1 \end{bmatrix} \begin{bmatrix} \sqrt{T_2} & i\sqrt{1-T_2} \\ i\sqrt{1-T_2} & \sqrt{T_2} \end{bmatrix} \begin{bmatrix} e^{i\theta(\vec{v})} & 0 \\ 0 & 1 \end{bmatrix} \begin{bmatrix} \sqrt{T_1} & i\sqrt{1-T_1} \\ i\sqrt{1-T_1} & \sqrt{T_1} \end{bmatrix} \quad (1.1)$$

The directional couplers in each MZI in the PNP operate with a design wavelength of 1570nm for 50:50 splitting. For this wavelength, therefore, we can substitute $T_1 =$

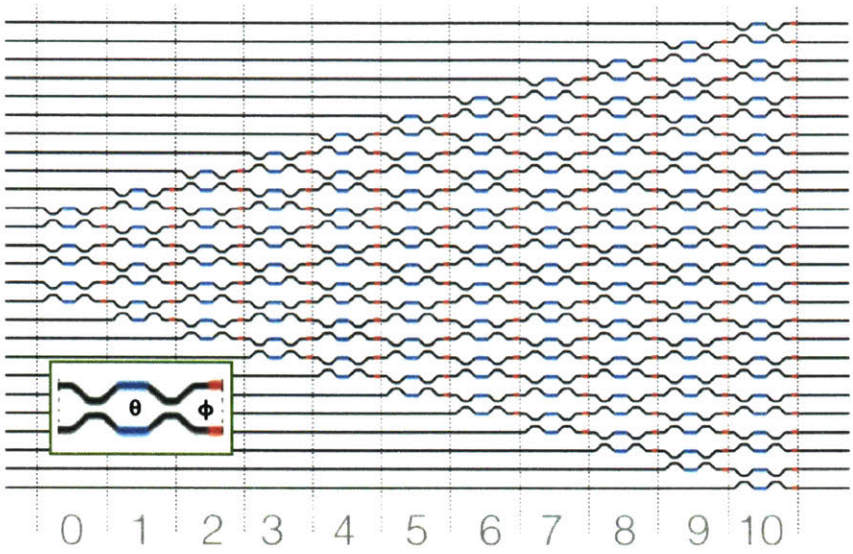

Figure 1-1: Programmable nanophotonic processor architecture fabricated in the silicon-on-insulator process (SOI). Waveguides are denoted by horizontal black lines, internal thermo-optic phase shifters are represented in blue, and external thermo-optic phase shifters are in red. Green inset shows a single MZI. Splitting ratio is controlled by internal phase difference θ. The external phase difference is ϕ. There are 11 layers total, capable of implementing a 26-mode unitary transform and a 9-mode arbitrary unitary transform.

$T_2 = \frac{1}{2}$ and rewrite the product in a form that is easily recognizable as a rotation matrix on the Poincare sphere.

$$
\begin{aligned}
T = & \quad \frac{1}{2}\begin{bmatrix} e^{i\phi} & 0 \\ 0 & 1 \end{bmatrix}\begin{bmatrix} 1 & i \\ i & 1 \end{bmatrix}\begin{bmatrix} e^{i\theta} & 0 \\ 0 & 1 \end{bmatrix}\begin{bmatrix} 1 & i \\ i & 1 \end{bmatrix} \\
= & \quad \frac{1}{2}\begin{bmatrix} e^{i\phi}(e^{i\theta}-1) & ie^{i\phi}(e^{i\theta}+1) \\ i(e^{i\theta}+1) & -(e^{i\theta}-1) \end{bmatrix} \\
= & \quad ie^{\frac{i\theta}{2}}\begin{bmatrix} e^{i\phi}\sin(\frac{\theta}{2}) & e^{i\phi}\cos(\frac{\theta}{2}) \\ \cos(\frac{\theta}{2}) & -\sin(\frac{\theta}{2}) \end{bmatrix}. \qquad (1.2)
\end{aligned}
$$

The transfer matrix of a single layer of the PNP - consisting of a vertical column of MZIs - is subsequently constructed as a block diagonal matrix of the individual MZI transfer matrices in that given layer. The total transfer matrix of the entire

PNP is then simply a product of the block diagonal matrices of each of the 11 layers.

$$T_{\text{PNP}} = T_{L11}T_{L10}T_{L9}...T_{L1} \tag{1.3}$$

Heaters

Reprogrammability of the PNP relies on individually controlling the internal and external MZI arm phase differences, θ and ϕ, for each MZI in the mesh. These phases are controlled via resistive heaters designed in the OpSIS process that make use of the strong thermo-optic effect in silicon [8, 9]:

$$\Delta\Phi = \left(\frac{2\pi L}{\lambda_0}\right)\left(\frac{dn}{dT}\right)\Delta T, \tag{1.4}$$

where $L = 61.6\mu m$ is the length of the heater, λ_0 is the vacuum wavelength of guided light, and $\frac{dn}{dT} = 1.86 \times 10^{-4}$ K^{-1} is the thermo-optic coefficient of silicon at 300 K [8]. One can furthermore model the change in temperature, ΔT, as a function of the applied voltage across the heater [10]:

$$\Delta T = \frac{P\tau}{H} = \frac{V^2\tau}{HR_h}. \tag{1.5}$$

where P is the power dissipated across the heater, H is the heat capacity, τ is the thermal time constant, and R_h is the resistance of the integrated silicon heater. Therefore, it follows that the phase shift implemented by a single heater follows a square-law relationship with the applied voltage across its terminals

$$\Delta\Phi = \left(\frac{2\pi L\tau}{\lambda_0 HR_h}\right)\left(\frac{dn}{dT}\right)V^2. \tag{1.6}$$

Slight fabrication imperfections lead to random phase offsets, Φ_0, as well as slight variations in the heater resistances, R_h [11]. For the two fabricated PNPs used in the work presented in this thesis, the heater resistances were measured to be $R_h = 835.9 \pm 12.7\Omega$ and $R_h = 836.1 \pm 12.9\Omega$. In Chapter 3, we will present calibration routines used to characterize the phase offsets, as well as individual heater performance as a

function of voltage for each of the heaters in the PNP.

Programming arbitrary unitary matrices

Individual control of each of the phase shifters in the PNP affords us the ability to produce a 26×26 transform with 176 degrees of freedom. However, these transforms take on a very particular form, given by the product calculated in (1.3). In 1994, Reck *et al.* derived a protocol for realizing any unitary matrix on a mesh of linear optical components: beam splitters, phase shifters, and mirrors [1]. The protocol relies on a recursive factorization technique, in which one can successively zero out each of the $\frac{N(N-1)}{2}$ off-diagonal elements in the unitary by applying a series of rotation matrices. These rotation matrices can be implemented experimentally using MZIs, as we can see from (1.2) where the directional coupler MZI applies a rotation on two modes. The general protocol is outlined in Figure 1-2 for a unitary of dimension 4.

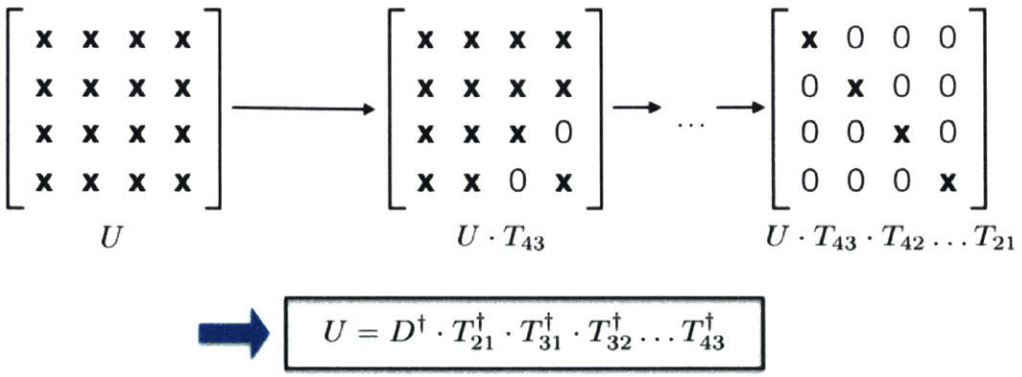

Figure 1-2: Recursive factoring technique for decomposing a unitary into linear optical components using the protocol developed by Reck *et al.* [1]. Here, T_{ij} refers to an MZI that interferes spatial modes i and j.

The structure of the linear optic network that implements the product in Figure 1-2 is a triangular mesh of MZIs, shown on the left in Figure 1-3, where each crossing represents one MZI. It follows that, using this decomposition scheme, light routed through the lower modes passes through more MZI layers than light in the higher modes, resulting in path-dependent loss. To counteract this issue, Clements *et al.* [2]

reformulated the factoring technique to zero out the off-diagonal terms in the unitary in a different order, enabling the mesh to be encoded in a square configuration, rather than a triangular one (right side of Figure 1-3).

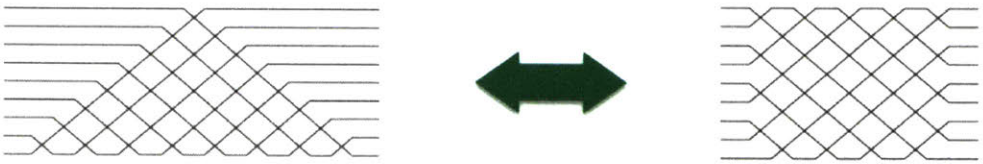

Reck *et al.*, 1994 Clements *et al.*, 2016

Figure 1-3: Comparison of Reck and Clements unitary decomposition architectures. The linear optical decomposition given by the Reck scheme is triangular with path-dependent losses, while the Clements scheme is square and is resistant to path-dependent losses. Figure adapted from [2].

This encoding requires that the circuit be run in reverse (i.e. from right to left). So in order to apply this decomposition in the PNP, one must instead decompose the Hermitian conjugate, $U^\dagger$, of the desired unitary operator, U. Table 1.1 contains a comparison of the resource requirements of the two encoding schemes. We observe that the maximum unitary size that one can encode on the PNP is 9 for the Clements scheme and only 7 for the Reck scheme. This advantage in spatial efficiency as well as robustness to path-depended losses motivate our choice to use the Clements scheme for all unitary decompositions presented in this thesis.

Encoding	**Encoding Layers**	**MZIs**	**max(N_{PNP})**
Reck [1]	2N-3	$\frac{N(N-1)}{2}$	7
Clements [2]	N	$\frac{N(N-1)}{2}$	9

Table 1.1: Comparison of unitary decomposition protocols for linear optics. Here, N refers to the dimension of the desired unitary matrix to be encoded, and max(N_{PNP}) is the maximum dimension of a unitary matrix that can be encoded on the OpSIS PNP we consider in this thesis.

1.2 PNP as a transceiver

1.2.1 Channel structure

In its most basic form, a communication channel is made up of an encoder, a decoder, and a physical channel over which information is sent [12].

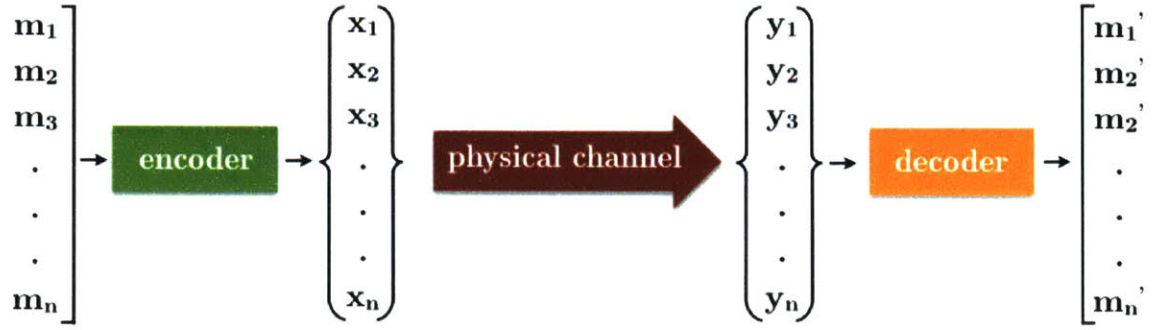

Figure 1-4: Basic structure of a communication channel. Messages $\{m_i\}$ are encoded into codewords $\{x_i\}$, sent across a physical channel, and the received codewords $\{y_i\}$ (which under ideal conditions are the same as $\{x_i\}$) are decoded back into the original set of messages.

Ever since it was proposed by Forney in 1965 [3], the concatenated code channel structure (Figure 1-5) has formed the basis of communications protocols operating on limited resource budgets, such as those used in space communication until the 1980s, and capacity-approaching turbo codes developed in the 1990s [13]. By combining the traditional (inner) encoder and decoder with an additional outer encoder and decoder, one can achieve exponential improvements in error probabilities while maintaining a coding/decoding complexity that is still polynomial with the block length [3]. We will be focusing on the physical implementation of the superchannel using PNPs as the inner encoder and decoder in this thesis.

1.2.2 Channel metrics

One of the main metrics for calculating the performance of a channel is the mutual information [12]. This measure gives insight on how much one can learn about a

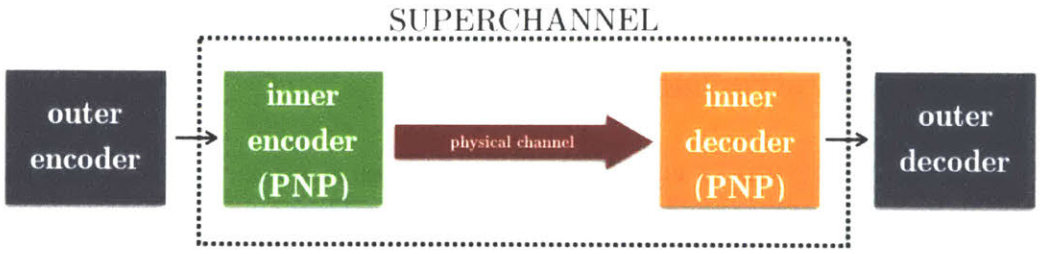

Figure 1-5: Concatenated coding architecture. A superchannel consists of the inner encoder, physical channel over which the information is sent, and the inner decoder. An outer code serves to boost channel capacity by mitigating errors and maintaining a resource complexity that scales polynomially with block length [3].

random variable Y by having information on another variable X:

$$I(X;Y) = \sum_{x\in\{X\}}\sum_{y\in\{Y\}} p(x,y)\log\left(\frac{p(x,y)}{p(x)p(y)}\right) \tag{1.7}$$

$$= \sum_{x}\sum_{y} p(y|x)p(x)\log\left(\frac{p(y|x)}{\sum_x p(y|x)p(x)}\right) \tag{1.8}$$

In a communication channel, the sender, Alice, sends a codeword from a set of codewords {X}. The receiver, Bob, receives a codeword from a set {Y}. Ideally, by knowing what message Alice sent, one would uniquely know what message Bob receives. However, in realistic channels, this is not always the case. In this thesis, the measure used to quantify the performance of a physical implementation of the channel is the transition probability matrix, which is a matrix of the conditional probabilities [12]:

$$\mathbf{P} = \begin{bmatrix} p(y_1|x_1) & p(y_1|x_2) & \cdots & p(y_1|x_n) \\ p(y_2|x_1) & p(y_2|x_2) & \cdots & p(y_2|x_n) \\ \vdots & \vdots & \ddots & \vdots \\ p(y_n|x_1) & p(y_n|x_2) & \cdots & p(y_n|x_n) \end{bmatrix} \tag{1.9}$$

Using the measured transition probability matrix, one can then calculate the capacity of the channel by maximizing the mutual information over all prior probability

distributions, $p_x(X)$, either using Lagrange multipliers or constrained optimization [12]:

$$C = \sup_{p_x(X)} I(X;Y) \tag{1.10}$$

Considering a binary phase-shift keyed (BPSK) channel over multiple modes, another metric of particular significance to links with constrained photon budgets is the *photon information efficiency*, which quantifies the information capacity per received photon [14]:

$$\text{PIE} = \frac{C(N_R)}{N_R} = \frac{Mg(\bar{n})}{M\bar{n}} = \frac{(1+\bar{n})\log(1+\bar{n}) - \bar{n}\log\bar{n}}{\bar{n}} \tag{1.11}$$

where N_R is the mean received number of photons, M is the number of separate modes in the channel, and $g(\bar{n})$ is the Holevo-limited channel capacity of a single-mode lossy bosonic channel with mean photon number $\bar{n}$ [14].

1.2.3 Joint detection receivers in telecommunications

Space-based communication systems additionally require reliable communication over photon-starved links, since photons are often lost over long propagation distance [15]. The current state of the art is a download rate from the moon to Earth of 622Mbps and upload rate of 20 Mbps, achieved by the NASA Lunar Laser Communication Demonstration (LLCD) [16]. This system uses a pulse-position modulation encoding with a capacity-approaching turbocode decoder. Pulse-position modulation (PPM) is an ideal encoding scheme for establishing communication over lossy links with limited optical output power. Theoretical work has been done to describe the design of an interferometric receiver called the "Green Machine" that converts a coherent signal distributed across many modes into a PPM signal that approaches the Holevo quantum channel capacity with increasing mode size [14].

Comprised as an array of variable-ratio beam splitters, the programmable nanophotonic processor (PNP) chip described in this thesis is one architecture for implement-

ing a Green Machine receiver to enable Holevo-limited PPM communication over photon-starved links. In addition, the dynamic tunability of the PNP, in theory, allows for corrections of channel imperfections on time scales longer than the program times of the active on-chip components. These types of joint-detection receivers are ideal for the low mean-photon number regime because they are capable of achieving superadditive classical channel capacity; that is, the capacity of a channel over m modes is greater than or equal to the capacity of m single-mode channels [14, 17]. The photon information efficiency for different mode sizes for a BPSK-Green Machine channel that considers the erasure outcome from loss is shown in Figure 1-6. One can see that as the mean photon number decreases, the PIE approaches the maximum value for the specified number of modes.

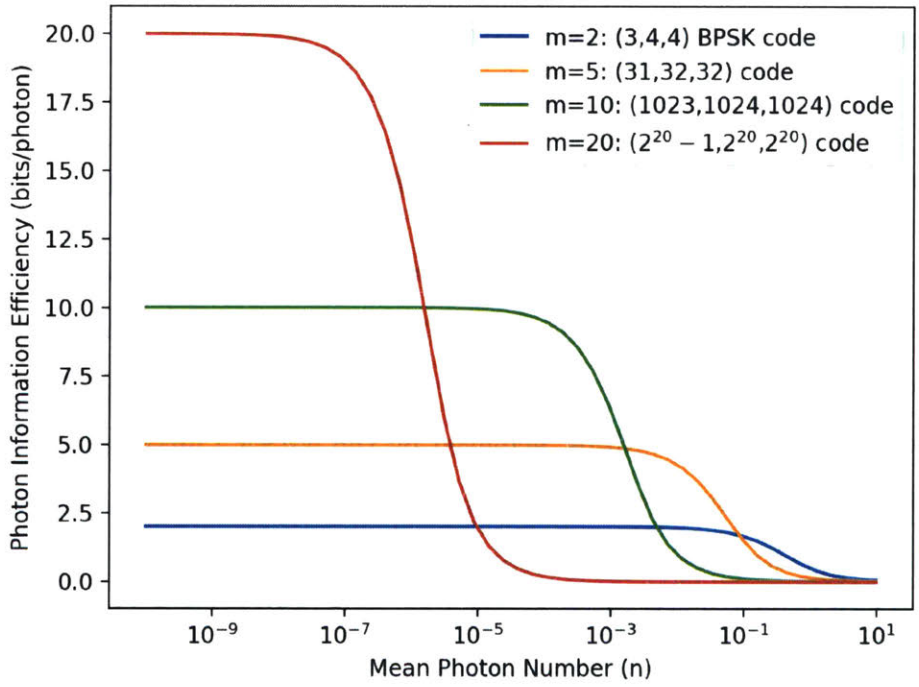

Figure 1-6: PIE as a function of mean photon number for different BPSK Green Machine sizes.

Chapter 2

Setup

A system diagram of the PNP along with key control hardware is shown in Figure 2-1. Coherent light is input to the chip from a tunable near-infrared Santec TSL-710 semiconductor laser. The integrated waveguide structure only supports transverse-electric (TE) electromagnetic modes, so a polarization rotator is used to rotate the polarization of light from the laser into TE polarization for maximum coupling into the chip. Additional engineering details and considerations are presented in the following section. Individual control of each of the 176 thermo-optic phase shifters integrated onto the chip is implemented with a chain of control electronics interfaced to the chip via gold wirebonds. These wirebonds route between signal pads on the control PCBs and electrical pads fabricated onto the chip.

2.1 Input/Output Coupling

The goal for all coupling solutions presented is to be able to interface standard 127μm pitch, 10μm mode-field-diameter (MFD) telecommunications fiber arrays with the input and output of the PNP. Traditional ultra-high numerical aperture (UHNA) and lensed fiber arrays both have very short working distances and, thus, require very close coupling distances to the chip. As a result, small vibrations or instabilities pose

Setup work was done in close collaboration with Nick Harris.
Free space lens setup was built in collaboration with Max Tillmann.

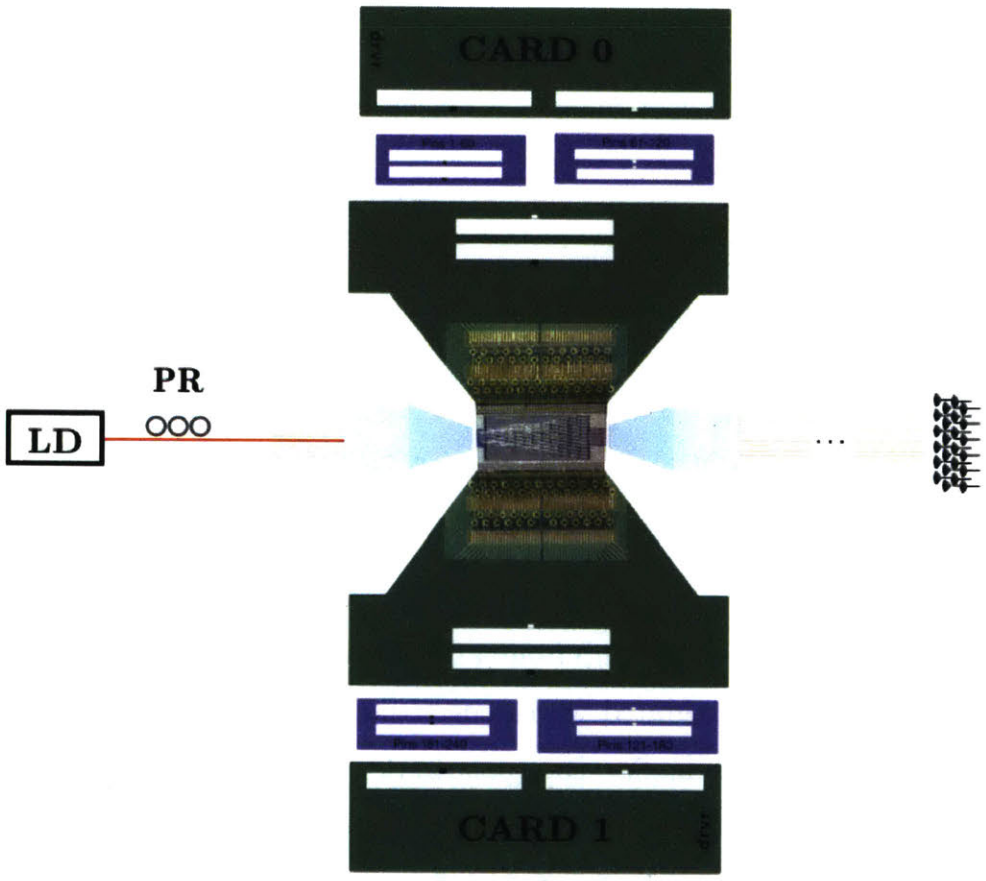

Figure 2-1: Experimental system components for OpSIS programmable nanophotonic processor chip. Light at 1570nm is rotated into TE polarization and coupled to the input of the PNP chip via a laser-written glass interposer fanout chip. Output light is routed to an array of InGaAs photodiode readout circuits. Tunability is achieved via the voltage-controlled thermo-optic phase shifters.

a significant risk of damaging the chip facet. Alternative fiber array solutions can involve gluing the arrays directly to the chip, however, these solutions are permanent and require very precise thermal and mechanical stability during the curing phase of the glue, as well as in the setup, to minimize stress on the joint. The pitch and MFD of the PNP were scaled down from the standard 127μm and 10μm, respectively, by a factor of 5 in order to enable a free-space coupling interface that uses safer long working-distance NIR objectives instead of fiber arrays.

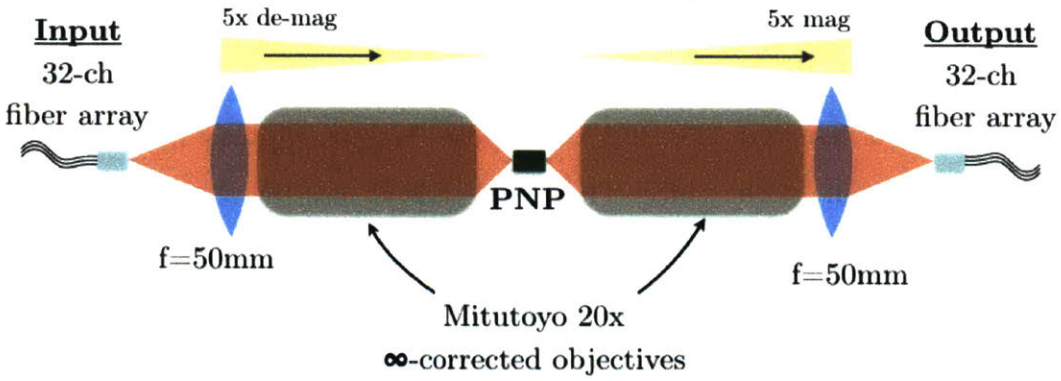

Figure 2-2: Lens-based free space coupling schematic for imaging Gaussian modes from a 26-mode telecommunications fiber arrays to the facets of the PNP.

2.1.1 Free-space coupling approach

The initial design incorporated an ∞-corrected 20x NIR objective from Mitutoyo. This objective features a tube lens with focal length f=200nm, so when combined with a C-coated aspheric lens with a focal length of f=50mm from Thorlabs (AL2550-C), one can obtain a magnification of 5x. However, due to transmission losses inside the objective of approximately -1.5dB for 1550nm, clipping of the collimated beam by smaller aperture lenses within the objective, and distortion of the beam due to surface irregularities of the f=50mm eyepiece lens, the maximum coupling that was achieved using this approach was approximately -25dB per facet.

The objective was replaced by another f=10mm aspheric C-coated lens from Thorlabs (AL1210-C) in an effort to mitigate coupling losses. A theoretical coupling loss of -0.2dB per facet due to lens absorption and reflection losses was expected for this system. However, the 60-40 scratch-dig (a parameter quantifying the surface irregularity of the lens) of the two coupling lenses distorted the Gaussian beam so that the maximum coupling efficiency that could be achieved was -12.5dB loss per facet.

2.1.2 Glass interposer chips

Laser-written glass waveguide interposer chips were custom fabricated by TEEM Photonics as an alternative to lossy free-space coupling approaches. A fanout chip (Figure 2-3) was designed to interface between a standard polarization-maintaining

(PM) 127μm pitch, 10μm MFD fiber array and the 24.5μm pitch, 2μm MFD of the waveguide modes at the chip facets. Each interposer guides 26 spatial modes with optical crosstalk of less than 25dB. An interposer fanout chip was used both at the input and the output of the chip. The characterized insertion loss for each of the modes from the device data sheet is listed as falling within the range of 0.61dB-0.87dB for one of the interposers and 0.47db-0.50dB for the other. Steel fiber array mounts were custom designed to position each fiber array with 5 degrees of freedom on a combination of a 3-axis Thorlabs NanoMax stage and a Thorlabs PY004 pitch/yaw stage.

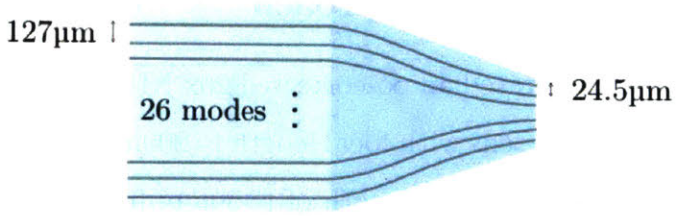

Figure 2-3: Laser-written glass interposer fanout structure manufactured by TEEM Photonics for coupling between 127μm pitch telecom fiber array and 25.4μm pitch chip facets.

2.2 Electrical control

Heater driver boards were constructed to control the voltage applied to the thermal phase shifters on each arm of the MZIs on the PNP. There are a total of 240 channels divided between two printed circuit board (PCB) driver boards that are individually controlled via a Teensy Arduino microcontroller, which controls a series of digital-to-analog controllers (DACs) [18]. Test switch boards were also built as a prototyping step so that one can choose whether each individual pad on the chip is connected to the signal chain and can receive voltage, or if it is connected to ground and the signal chain is left open.

The voltage signal chain from the printed circuit driver boards are routed onto the chip via gold wirebonds to electrical contacts on the chip. Previously, mechanical

probe arrays were used to contact the on-chip electrical pads. However, mechanical instability of the probe tips resulted in time-dependent contact resistance, which introduces error in the heater phase-voltage relationships necessary for high-fidelity control. Wirebonding ameliorates this issue and reduces alignment error and overhead.

2.3 Detection

Information on the PNP is encoded in the amplitude and phase of light in the waveguide modes. Therefore, a series of photodiode circuits were constructed to measure the intensity of light at the output of the chip [18]. The photodiodes used were InGaAs p-i-n photodiodes with a responsivity of approximately 0.93 A/W at 1550nm and a 2GHz cutoff frequency manufactured by Precision Micro-Optics. The setup to calibrate the photodiode array used for detecting the intensities at the output of the chip is shown in Figure 2-4(a). The goal is to convert the raw voltage output of each photodiode circuit to an optical power reading that can be programmed into the photodiode array firmware.

In photoconductive mode, the current and voltage response of each photodiode will increase linearly with input optical power between the noise floor and saturation points [19]. A sweep was done of the input optical power incident on each photodiode in the array in order to create linear fit relations for the linear regions of operation. The fit for photodiode 3 of the array is shown in Figure 2-4(b). One can also determine from these plots that the optical power needed to saturate the detector is appoximately 20μV.

2.4 Thermal control

Temperature stability is a critical requirement for the PNP system, not only because all active control on the chip is implemented via the thermo-optic coefficient in silicon, but because coupling efficiency for Gaussian beams to and from the chip

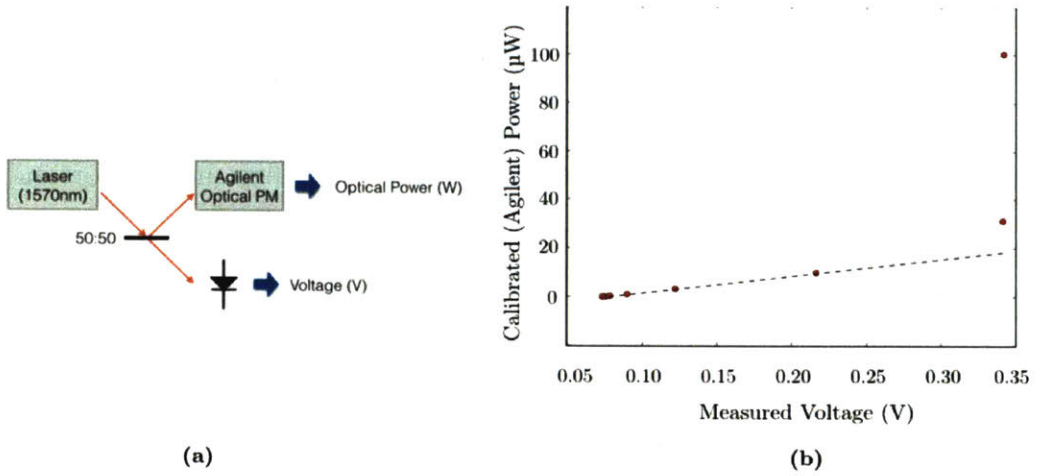

Figure 2-4: (a) Characterization setup for photodiode voltage readout. (b) Photodiode response in photoconductive mode, with saturation power seen at approximately 20μW.

decreases exponentially with the slight misalignment that can arise due to thermal expansion.

To stabilize the global temperature of the PNP, the chip was mounted on a copper block with thermally conductive glue. A thermistor mounted on the chip chassis measures the temperature on the chip, and a Peltier cooler glued to the copper block applies a temperature change. Both these components are connected to a Thorlabs p-i-d temperature controller to maintain the temperature at a value within 0.01 Kelvin. Finally, a heat sink is glued to the bottom of the Peltier cooler for increased surface area. Depending on the PCB grounding configuration, the aluminum chassis and copper block interface would need to be shielded with insulating tape to avoid creating a thermocouple between the different metals.

Chapter 3

PNP Calibration

Imperfections in waveguide geometry, free-carrier absorption in doped silicon regions, and inaccuracies in voltage controls introduce non-idealities such as unbalanced beam splitting, propagation loss, and phase shift errors, respectively [8]. These disorder terms diminish the fidelity of quantum operations performed on the PNP, so different schemes were investigated to determine the realistic unitary of the PNP by extracting the real beam splitting ratios, propagation losses, and phase shift errors given only the input state and output state of the processor.

3.1 Loss Mode Model

There are three main sources of disorder that were considered when constructing a disordered MZI model for the PNP: unbalanced beam splitting ratios due to variations in waveguide geometry, propagation loss due to free-carrier absorption in doped regions in the thermal phase shifters, and phase shift errors due to inaccuracy in the operation of the voltage-controlled thermal phase shifters [8]. The transmission of each beam splitter was pseudo-randomly generated from a Gaussian distribution with a mean of 0.5 and a standard deviation of 0.043 [6]. Photon loss that occurs as a result of propagation through a thermal phase shifter can equivalently be modeled

Characterization in the latter half of this chapter was done in collaboration with Nick Harris. Crosstalk measurements were made with Jacques Carolan.

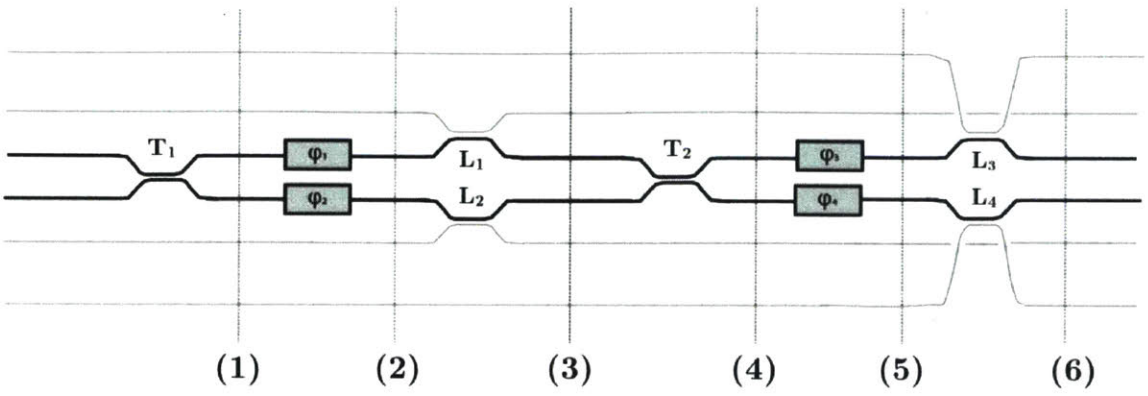

Figure 3-1: Model of a lossy MZI. Outer four waveguides represent "loss modes", and central two waveguides represent the physical waveguides in the MZI. Loss is modeled by light coupled out of the waveguide with a given "loss transmission", L, that is characteristic of the material.

by an additional directional coupler, coupling light in the original arm to an initially empty "loss mode". Given a measured insertion loss of 0.23±0.13 dB [6], the transmission ratio for the loss directional couplers was modeled by a Gaussian distribution with a mean of 0.9484 and a standard deviation of 0.0284.

3.1.1 Nonlinear optimization for characterization

Python simulation software developed for the PNP was used to model the function of all aspects of the processor given the following user-specified inputs: beam splitting ratios, propagation losses, and phase shift errors. Behavior of different sized sections of the chip were modelled, down from the single-MZI level to the MZI layer level to the entire chip level. Non-ideality parameters were then modeled using randomly generated values derived from appropriate Gaussian distributions centered about ideal values. We attempted to determine these randomly generated parameter values using the nonlinear optimization method of Multi-Level Single-Linkage (MLSL) global optimization with various local optimization algorithms, including Bound Optimization by Quadratic Approximation (BOBYQA), Constrained Optimization by Linear Approximation (COBYLA), Nelder-Mead Simplex, and Sublex [20, 21, 22, 23, 24, 25].

Starting with an initial guess for the variation parameters given by the ideal values (means of the Gaussian distributions mentioned in the previous section), MLSL

global optimization was used in conjunction with the various local optimizer algorithms listed above to try to extract the true variation parameters of a randomly generated PNP in simulation, using only user-controlled inputs and the corresponding simulated outputs. This is a fair model for what one could measure experimentally on a physical PNP chip, as one cannot measure any of the internal parameters such as beam splitting ratios or insertion losses of individual components of the PNP once it has been fabricated.

By setting the objective function of the optimization to be the Frobenius norm of the vector difference between the true simulated output values and the output values generated using the guess parameters of the current optimization step, one can determine how accurately the guess parameters at the specified optimization step describe the true non-ideality parameters within the PNP. In order to account for differences in optimization efficacy that may arise as a result of using different input vectors, the simulation transform calculated for the PNP was expanded fivefold to simulate five identical PNP instances acting on five different input vectors at once, for each given optimization instance.

3.1.2 Optimization Results

A verification step was executed upon completion of each optimization to check whether the optimization did, in fact, generate a more accurate description of the true PNP parameters than the initially guessed ideal parameter vector.

In this step, two vector differences were calculated: (1) the difference between the optimized and the true non-ideality parameters and (2) the difference between the initial guess parameters and the true parameters. The optimization was considered to be effective if the optimized vector difference had a consistently smaller magnitude than the initial guess vector difference. In other words, the parameters were closer to being correct after the optimization than they were at the start. The resulting vector differences from 25 optimization trials for MLSL global optimization paired with BOBYQA and with Nelder-Mead local optimizers are shown in Figure 3-2.

We can see that the optimized vector differences of the PNP parameters were not

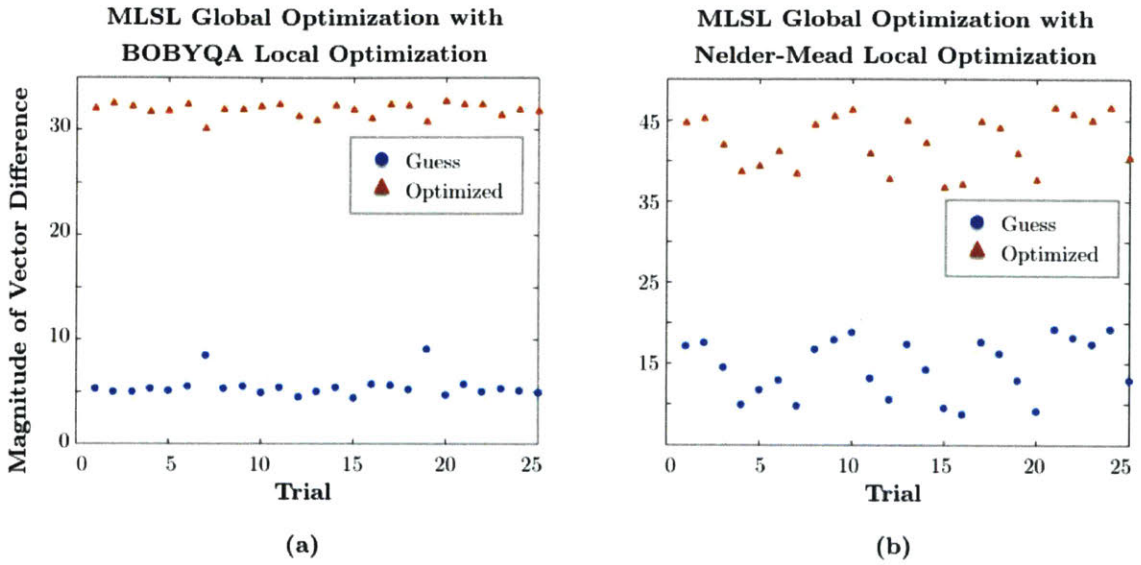

Figure 3-2: Results from BOBYQA and Nelder-Mead local optimizers using MLSL global optimization. Red triangle markers indicate optimized vector difference magnitudes and blue circle markers indicate initial guess vector difference magnitudes. Optimized vector differences were consistently greater than guess differences, indicating that optimization was ineffective.

even less than those of the initial guess parameters, indicating that the optimization was unsuccessful. It is important to remember here that this vector difference was not the objective function with which the optimization was run, so it makes sense that the optimizer could end with a vector difference greater than that of it's starting guess. It appears that this approach involves optimizing over too many variables, resulting in an abundance of incorrect local minima.

3.2 Experimental Calibration

As we saw in the previous section, we cannot use a simulation model to back out the individual values of each parameter that contributes to the expression for the MZI transfer matrix. However, by relaxing our focus on characterizing every source of non-ideality on the chip, we can observe from (1.2) that there are only two basic degrees of freedom to characterize within each MZI: the internal phase shifter θ and the external phase shifter ϕ. By characterizing the response of each of these knobs

on the PNP, we can determine what phases are necessary to implement an arbitrary unitary transform that we desire. The characterization protocol for the internal phase shifters is distinct from that of the external phase shifters, and both are detailed in the following subsections.

3.2.1 Internal phase shifter calibration

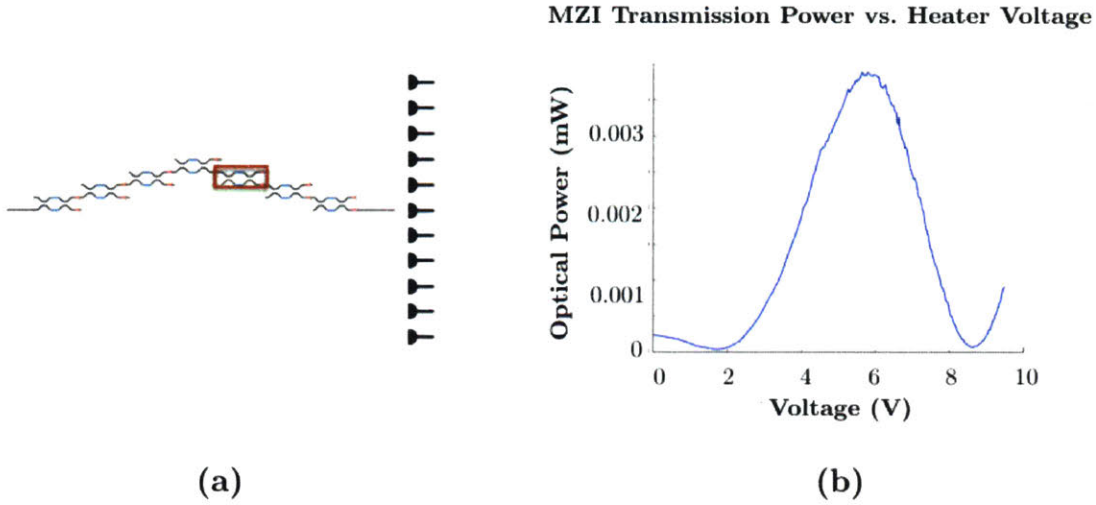

Figure 3-3: (a) Calibration protocol for extracting phase vs. voltage relationship for MZI internal phase shifters. For a given MZI (boxed in red), a wire is routed from the chip input (output) to the MZI input (output). The internal phase shifter voltage is swept between 0V and 10V and optical transmission is measured at the output. (b) Example transmission vs. voltage fringe seen at detector when calibrating the internal phase shifter.

The general protocol for calibration of the internal phase shifters relies on our knowledge of the transmission function of the MZI. For light input in the top arm and detected from the top arm, for example, we can see from (1.2) that the measured intensity is given by the following expression.

$$I(\theta) = \left|\sin\left(\frac{\theta}{2}\right)\right|^2 \tag{3.1}$$

It is necessary to calibrate each internal phase shifter independently of all the others, so we first isolate an individual MZI by routing a wire to one of its inputs and from one of its outputs to a detector. Depending on whether the input/output routing

for the MZI accesses the top or bottom modes of the MZI, the intensity fringe will produce either a $\sin^2(\theta/2)$ or $\cos^2(\theta/2)$ curve. Combining this with our expression for the phase relationship as a function of voltage from (1.6) and an additional nonlinear term to model electron velocity saturation, we can fit each transmission fringe to achieve a relation $\theta(V)$ for each internal phase shifter, θ. Furthermore, once such a phase relationship exists, one can determine the voltage setting necessary to achieve a certain phase for each internal heater.

3.2.2 External phase shifter calibration

While it is fairly straightforward to observe a transmission signature that depends on the internal phase shifter setting, θ, we observe from the MZI transfer matrix in (1.2) that an intensity detected at the output of an individual MZI does not depend on the external phase shifter, ϕ. However, these phase shifters still play an important role in the interferometric decomposition of unitary matrices on the PNP [1, 2].

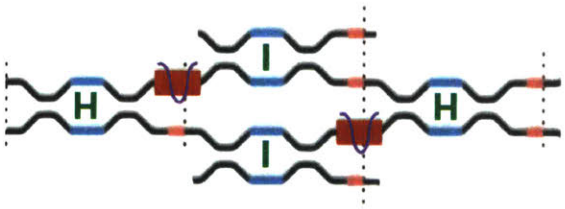

Figure 3-4: Meta-MZI configuration. A combination of four adjacent MZIs forms a meta-MZI with the top/bottom MZIs programmed to be identities and the left/right MZIs programmed to be Hadamard transforms. The internal phase difference of the meta-MZI is controlled by the difference in phase between the external phase shifter of the left and bottom MZIs.

One can still extract these signatures by programming 4 adjacent MZIs in the following configuration, thereby generating a meta-MZI that behaves like a traditional MZI, where symmetric beam splitters are implemented with Hadamard operations [26]:

$$H = \frac{1}{\sqrt{2}} \begin{bmatrix} 1 & 1 \\ 1 & -1 \end{bmatrix} \tag{3.2}$$

Our goal here is to normalize out relative phase differences between individual MZIs as a result of external phase shifters. To do this, we program each meta-MZI to perform a "swap" operation - equivalent to having an MZI internal phase difference of zero.

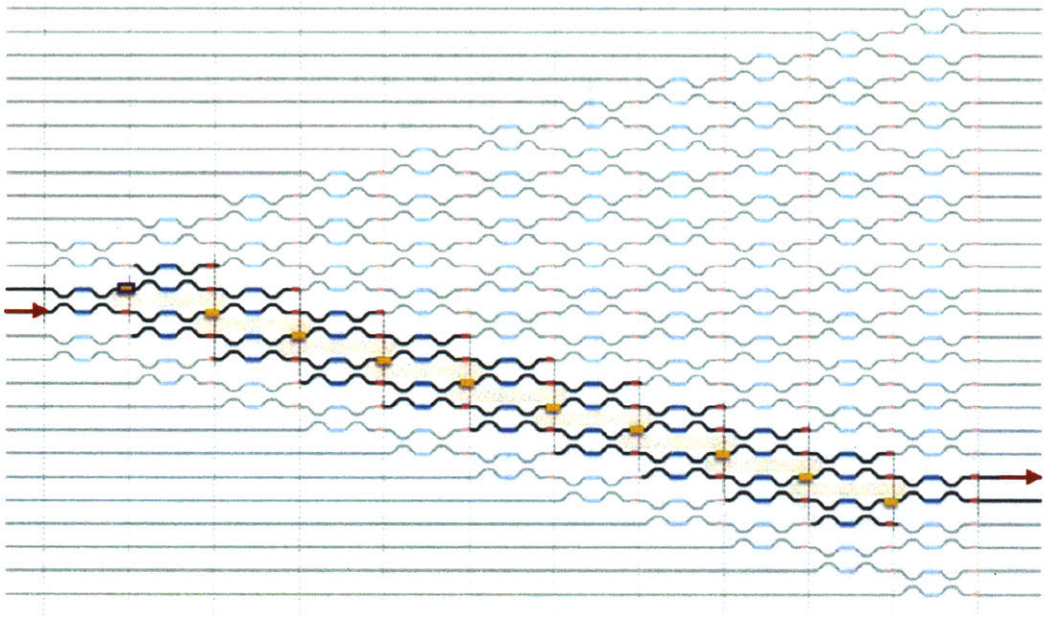

Figure 3-5: Meta-MZI calibration structure. Calibration is carried out in "chains", one of which is highlighted in the above figure. External phase shifter voltages are swept to generate transmission fringes for the entire chain of meta-MZIs, which can be processed to determine external phase vs. voltage relationship and offsets.

We only consider the top external phase shifter for all MZIs, since the bottom phase shifters are redundant and cannot be controlled electrically. Therefore, for each meta-MZI, there are two variable external phase shifters (shown as yellow blocks in Figure 3-5) and two constant phase shifts inherent to the structure, which will be described in the following paragraph. Since adjacent meta-MZIs share a phase shifter, this generates a system of m coupled equations in m variables, where each meta-MZI chain has one phase shifter (denoted in Fig 3-5 by the top yellow box outlined in purple) that serves as a reference set to π, and

$$m = (\#\text{ meta-MZIs}) - (\#\text{ meta-MZI "chains"}) = 63 - 11 = 52 \tag{3.3}$$

is the number of non-reference external phase shifters in the PNP. For each meta-MZI, the following equation must hold in order for a swap to take place:

$$\phi_{\text{top}} - \phi_{\text{bottom}} + \phi_{\text{config,diff}} + \Delta = 0 \tag{3.4}$$

where ϕ_{top} and ϕ_{bottom} are the external phase shifters that are swept, $\phi_{\text{config,diff}} = \pi$ from the fact that the identity is implemented with a top arm phase difference of $(\theta, \phi) = (\pi, \pi)$, and Δ is the intrinsic phase difference between the two arms as a result of fabrication variations.

The constant phase difference, Δ, is determined from fitting the transmission sweeps of both ϕ_{top} and ϕ_{bottom} for a given meta-MZI and comparing the phase that results in maximum transmission for each sweep. Once we have taken sweeps of all the external phase shifters, calculated the Δ intrinsic phase difference for each meta-MZI, and set up the coupled system of equations, we can solve a simple matrix equation to determine the external phase offsets necessary to "zero" out the interference effects of fabrication imperfections on the external phase shifters. Using the fitted transmission sweeps for each external phase shifter, we can also use a protocol similar to that performed in the internal phase shifter calibration to extract a phase vs. voltage relationship for each individual external phase shifter.

3.2.3 Characterization

Once we have calibrated the phase response as a function of voltage for each of the individual phase shifters, we must determine how accurately we can implement a desired unitary transform on the chip. A unitary transform, defined as any matrix U that satisfies the condition $U^{\dagger}U = \mathbf{I}$, is a complex matrix with elements of the form

[26]:

$$U = \begin{bmatrix} r_{11}e^{i\theta_{11}} & r_{12}e^{i\theta_{12}} & \cdots & r_{1n}e^{i\theta_{1n}} \\ r_{21}e^{i\theta_{21}} & r_{22}e^{i\theta_{22}} & \cdots & r_{1n}e^{i\theta_{2n}} \\ \vdots & \vdots & \ddots & \vdots \\ r_{n1}e^{i\theta_{n1}} & r_{n2}e^{i\theta_{n2}} & \cdots & r_{nn}e^{i\theta_{nn}} \end{bmatrix} \tag{3.5}$$

Therefore, we observe that by measuring the amplitude and phase of each element in the unitary transform, we can obtain the full unitary that is applied on the chip. We can make these measurements in two steps, outlined in Fig 3-6.

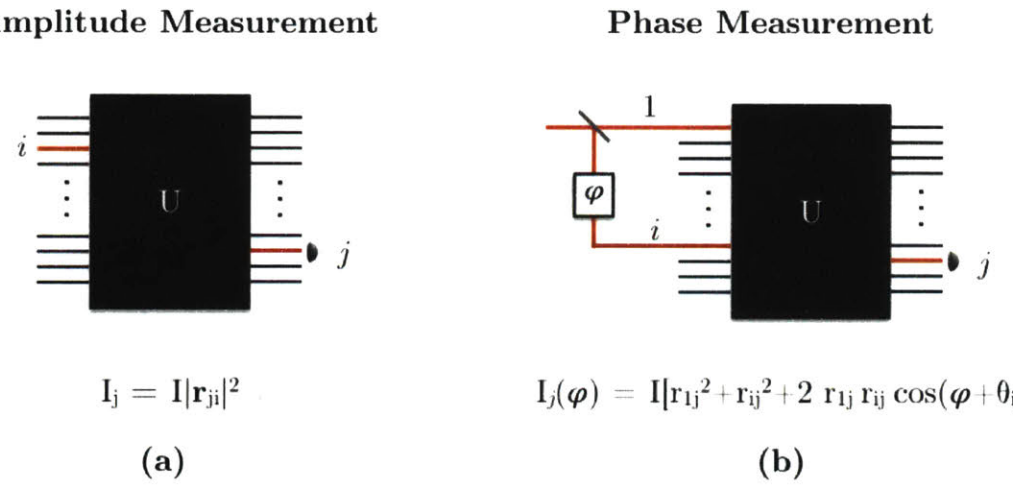

Figure 3-6: Unitary matrix characterization protocol. (a) Magnitudes can be measured directly using an intensity measurement at the detectors. (b) The phase of each element can be deduced from fitting an interference fringe detected at one output when two input modes are simultaneously illuminated.

For the amplitude measurement step, one can read off the magnitude of every element in column i by routing light with intensity I into the ith mode of the input. The measured power on the j^{th} detector I_j is given by $I_j = I|r_{ij}|^2$. Iterating through all input modes, i, and output modes, j, we can determine the magnitude r_{ij} of every element in the unitary matrix.

As with the external calibration step, measurement of the phases θ_{ij} is slightly more nontrivial because they do not present a distinct intensity signature without

some sort of interference. This interference is implemented using a protocol developed by Rahimi-Keshari *et al* [27] (outlined in Fig 3-6). We insert a coherent state input to the chip, program the MZI in the first layer to be a 50:50 beamsplitter, route the two resulting coherent states to input mode 1 and i of the unitary matrix circuit, and measure from output mode j while sweeping the value of ϕ. Without loss of generality, we can assume because the matrix is unitary and the columns and rows form a unitary basis, that the first column and first row of the matrix are real [27]. From here, we find the rest of the phases relative to these reference "borders". Measuring the optical power at output j with a given input phase difference ϕ results in the following intensity [27]:

$$I_j(\phi) = I\left|r_{1j} + r_{ij}e^{i(\phi+\theta_{ij})}\right|^2 = I[r_{1j}^2 + r_{ij}^2 + 2r_{1j}r_{ij}\cos(\phi+\theta_{ij})] \tag{3.6}$$

We then fit the fringe and find the value of ϕ that produces a maximum. Using this value, we can extract the phase θ_{ij} using the relation in (3.6). As a final step in the characterization, we normalize out the input and output coupling differences using an iterative normalization protocol described in [28].

3.2.4 Voltage Crosstalk Correction

While certain PNP programs, such as calibration routines for the internal and external phase shifters or routing wires, do not require accurate use of many MZIs at a time, programming an N-dimensional unitary matrix requires $(N)(N-1)$ phase shifters to be programmed simultaneously, not including those necessary for encoding border identities and input/output routing. When programming so many MZIs at once, it becomes necessary to consider the structure of the resistive network driving the thermo-optic phase shifters.

Each of the 176 phase shifters on the chip can be modeled as a quasi-constant resistor connected to the same ground terminal as all the other heaters. However, the ground terminal comprises of a network of physical metal pours both on the PNP chip and on the control PCB, leading to a small resistance between the heater grounds

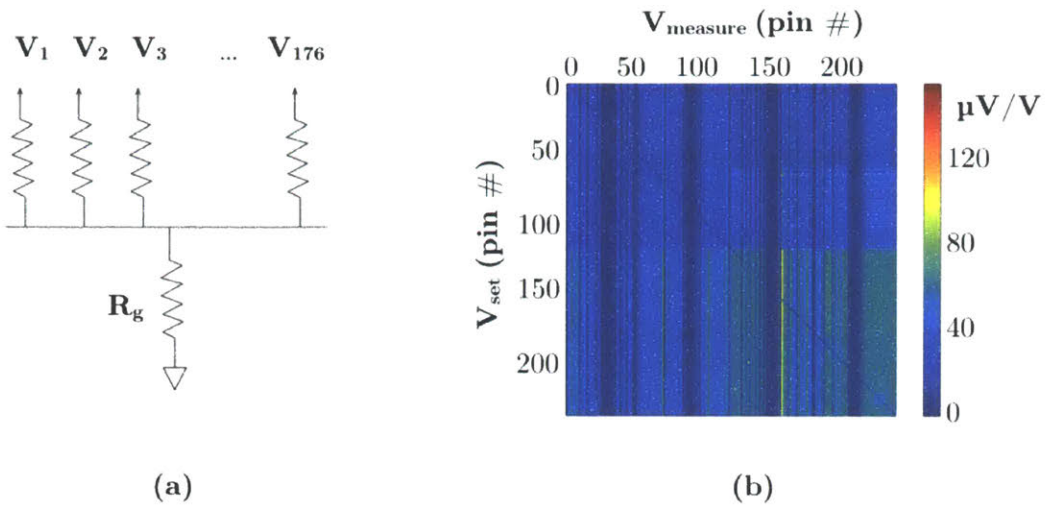

(a) (b)

Figure 3-7: (a) Voltage crosstalk model. A small ground resistance creates crosstalk that couples the voltages applied by all of the pins. (b) Measured linear correlation matrix quantifying crosstalk between all 240 pins.

and true ground (shown in Figure 3-7(a)). When a given heater is turned on, a small current flows through the ground resistor, changing the effective voltage drop across all the other resistors in the network.

To measure the effect of this ground resistance, one of the 240 voltage driver pins was probed while each of the other 239 pins was swept in voltage between 0 Volts and 7.0 Volts with 10 increments. This process was repeated for each of the 240 probe pins. A visualization of the linear fit gradient for each of these sweeps is shown as a correlation matrix in Figure 3-7(b). The voltage crosstalk curves were not perfectly linear, however, and the following paragraphs detail correction schemes assuming both a linear crosstalk model and a polynomial crosstalk model.

Linear Correction Model

Assuming a linear crosstalk model, we can write the desired voltage vector we would like to measure, $\vec{V}_{meas}$ as a function of the 240 voltages we need to set on the driver board, $\vec{V}_{\text{set}}$:

$$\vec{V}_{\text{meas}} = \overline{\overline{\mathbf{C}}}\vec{V}_{\text{set}} \tag{3.7}$$

$$\implies \quad \vec{V}_{\text{set}} = \overline{\overline{\mathbf{C}}}^{-1}\vec{V}_{\text{meas}} \tag{3.8}$$

After correction, we observe that low or zero desired voltage values in $\vec{V}_{\text{meas}}$ are corrected to negative values. The driver can only set positive voltages, so small ($-1\text{mV} < V_{\text{set,i}} < 0\text{V}$) negative values in the crosstalk-corrected voltage vector were rectified to zero. Values that were significantly lower than zero were programmed to throw an error, but this was rare.

The voltage crosstalk sweeps described in the previous section were repeated, this time with a corrected voltage vector for each voltage setting. Pin 71 had the highest measured crosstalk, so the sweep curves presented in the following sections were all conducted with pin 71 as the probe pin. The following table summarizes the voltage crosstalk slopes seen at pin 71 when sweeping a subset of the other pins.

Pin Set	**Uncorrected Grad.** ($\mu V/V$)	**Corrected Grad.** ($\mu V/V$)
All pins	30.4 ± 20.6	-0.191 ± 7.56
Excluding GNDs	30.3 ± 20.6	-0.0299 ± 7.46

We can see that the crosstalk correction indeed does work electrically to decrease the change in voltage of any given pin as a result of voltages applied on other pins. In order to determine if the correction provides an improvement optically, 276 random U(5) unitary matrices were generated using the following procedure:

$$\mathbf{C} = \text{random complex NxN matrix} \tag{3.9}$$

$$\mathbf{H} = \frac{1}{2}(\mathbf{C} + \mathbf{C}^{\dagger}) \tag{3.10}$$

$$\mathbf{U} = e^{(i\mathbf{H})} \tag{3.11}$$

For each of these random matrices, U, the characterization protocol described in Section 3.2.3 was carried out to determine the measured matrix, $\mathbf{U}_m$. Since we factor out the input and output coupling screens, the matrix we reconstruct is, in fact, unitary. Therefore, we use the following fidelity metric:

$$F = \frac{|\text{Tr}(\mathbf{U}_m^{\dagger}\mathbf{U})|}{N} \tag{3.12}$$

This is adapted from a similar non-unitary metric that takes into account losses [29]:

$$F = \left| \frac{\mathrm{Tr}(\mathbf{U}_m^\dagger \mathbf{U})}{\sqrt{N \mathrm{Tr}(\mathbf{U}_m^\dagger \mathbf{U}_m)}} \right|^2 \tag{3.13}$$

We then calculate the fidelity of the measured PNP matrix transform for all the randomly generated unitary matrices, both with and without the linear voltage crosstalk correction. Results are presented in a histogram in Figure 3-8.

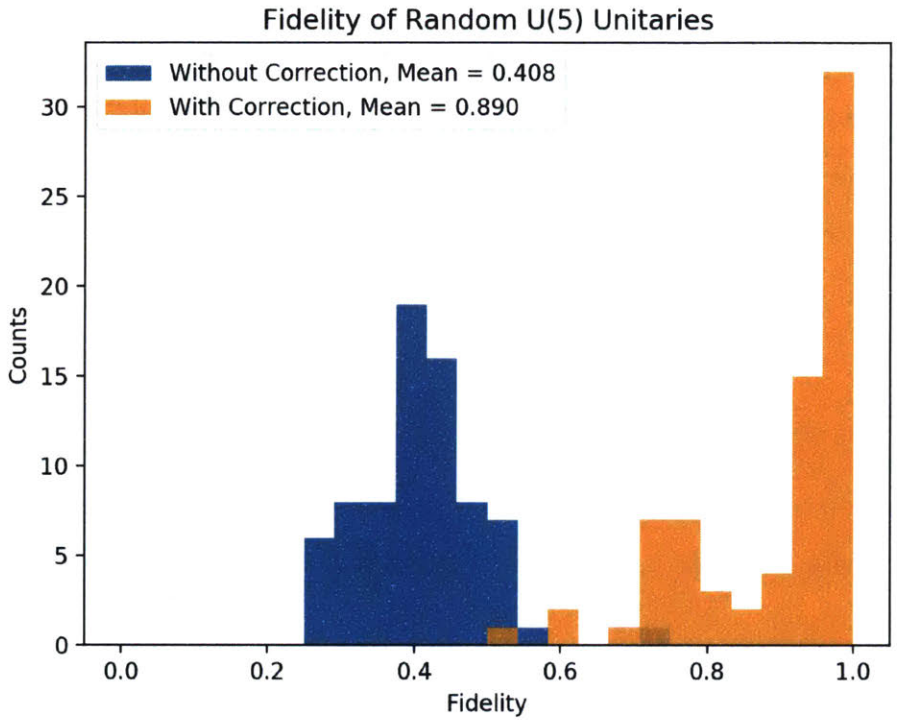

Figure 3-8: Fidelities of randomly generated U(5) unitary matrices with and without linear voltage crosstalk correction.

We observe a significant increase in fidelity after application of the voltage crosstalk correction algorithm. It is also worth noting, however, that there appears to be bi-modal distribution of the fidelities in the corrected scheme. One possible explanation is that certain unitary matrices are systematically incompatible with this approach. For example, when a unitary matrix is decomposed into its linear optical phases, if many of these phases are very small or zero, the corrected voltage vector in (3.8)

will have many negative values. These values are rectified to zero for compatibility with the voltage driver circuitry, which results in a deviation from the desired voltage vector. In addition, each pin in the voltage driver has a turn-on voltage around 0.12 V. As a result, the response of the pins in the (0V, 0.2V) range is highly nonlinear. If a desired unitary matrix requires setting many key phases with voltages within this range, then the linear solution approach will be incorrect even without rectification to zeros.

Polynomial Correction Model

Additional nonlinearity in the crosstalk curves is observed at high voltages. This could arise as a result of a temperature dependence of the heater resistances due to decreased carrier mobility with increasing temperature [30]. To account for these nonlinearities, we fit each crosstalk curve measured with a cubic function of the set voltages:

$$\vec{V}_{\text{meas}} = \overline{\overline{\mathbf{C}}}^{(1)}\vec{V}_{\text{set}} + \overline{\overline{\mathbf{C}}}^{(2)}\vec{V}_{\text{set}}^{2} + \overline{\overline{\mathbf{C}}}^{(3)}\vec{V}_{\text{set}}^{3} \tag{3.14}$$

Using Newton's method to approximately solve this system of cubic equations, we can obtain an iterative solution to $\vec{V}_{\text{set}}$ that produces within a user-specified tolerance, ϵ, a measured voltage vector matching the desired measured voltage vector [31].

We then repeat the voltage sweeps using the polynomial crosstalk correction with pin 71 as the probe pin. Again, fitting the curves to a linear function to see if the crosstalk signature is still present, we observe the slopes in Figure 3-9.

The following table summarizes the same data for these 10 random pins as the data shown for the linear model. It appears that the polynomial crosstalk correction does help, but more pins need to be tested in order to make an accurate comparison with the data from the linear crosstalk correction.

Pin Set	**Uncorrected Grad.** $(\mu V/V)$	**Corrected Grad.** $(\mu V/V)$
All 10 pins	25.0 ± 23.7	-4.20 ± 4.95
Excluding GNDs	25.8 ± 25.0	-3.42 ± 5.16

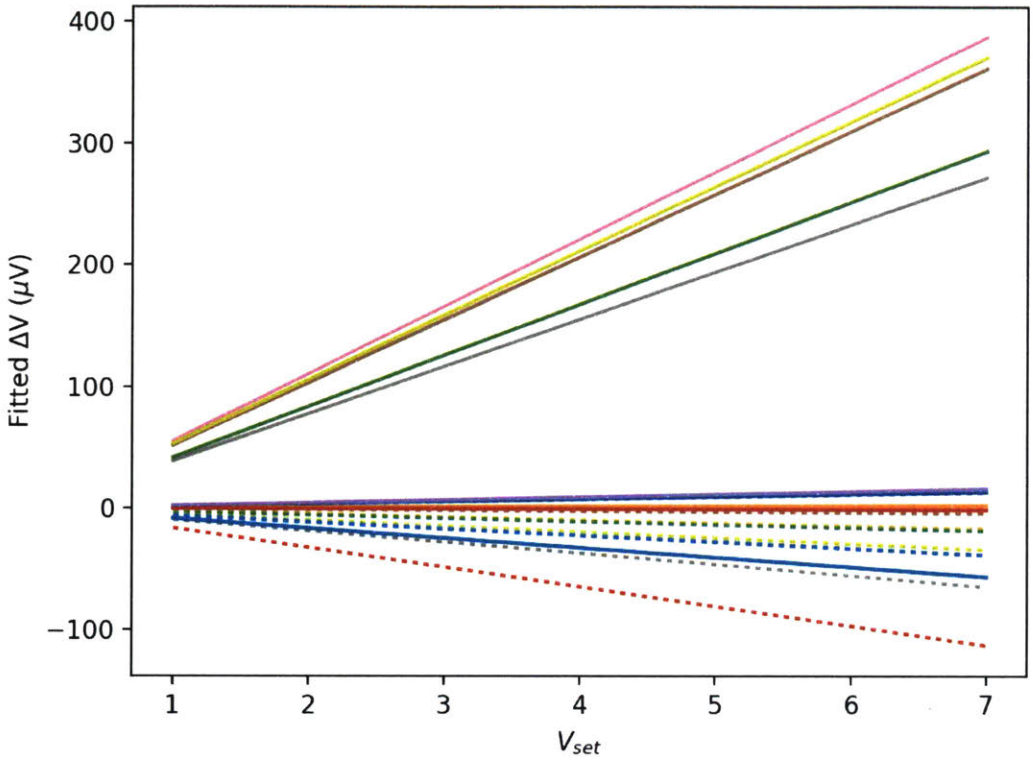

Figure 3-9: Linear fits of voltage sweeps of 10 random pins while probing pin 71. Solid (dotted) lines represent fitted slopes of sweeps without (with) polynomial crosstalk correction.

Chapter 4

U(4) Green Machine Superchannel

For the demonstration presented in this thesis, we will be focusing on a PNP implementation of a Green Machine superchannel for superadditive channel capacity when used with a concatenated coding scheme. There are three parts of the channel that, taken together, form the superchannel of a concatenated coding protocol: the transmitter (Alice), the joint-detection receiver (Bob), and the channel over which messages are sent from Alice to Bob. A schematic of the multiple spatial mode structure of the channel is shown in Figure 4-1.

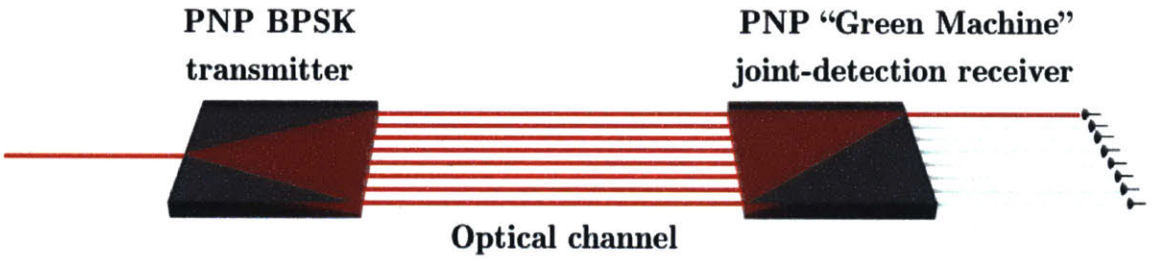

Figure 4-1: Schematic of PNP Green Machine channel.

For a positive integer m, a $(2^m, 2^m, 2^{m-1})$ PPM code is equivalent via application of a Green Machine unitary transform to a $(2^m - 1, 2^m, 2^{m-1})$ BPSK code, where an (n, K, d) code represents an encoding protocol where n is the length of the codewords, K is the number of words in the code set, and d is the Hamming distance [14]. The PNP is naturally configured for spatial mode manipulation, and we consider a BPSK code for the work presented in the rest of this chapter.

4.1 Transmitter

For initial demonstrations, we will be transmitting a (3,4,2) BPSK code. A (1,2,1) BPSK code transmitter on the PNP is simply a single MZI with phase settings $(\theta, \phi) = (\frac{\pi}{2}, 0)$, which is a trivial application. By illuminating either the bottom or top input port, one can choose between the two codewords: {+, -}. To implement an $m = 2$ (3,4,2) BPSK transmitter, however, one must be able to transmit any of 4 codewords given by the columns of a 4-dimensional generalized Hadamard matrix [26]:

$$\mathbf{H}_4 = \frac{1}{2}\begin{bmatrix} 1 & 1 & 1 & 1 \\ 1 & -1 & 1 & -1 \\ 1 & 1 & -1 & -1 \\ 1 & -1 & -1 & 1 \end{bmatrix} \tag{4.1}$$

These codewords can be implemented in two ways on the PNP: (1) as a unitary matrix decomposition or (2) as a binary tree. The design and implementation of these two methods, along with preliminary performance data are described in the following subsections.

4.1.1 Unitary transmitter

The unitary matrix decomposition for $\mathbf{H}_4$ is implemented using the square Clements protocol [2], which uses 4 layers of the PNP. Selection of the codeword i is achieved by illuminating the i^{th} spatial mode at the input of the square transmitter circuit. In order to completely automate the codeword selection process and minimize errors due to uncontrollable global phase differences at the input, two layers are used as routing at the input, with only one chip input illuminated at a time. The configuration of the MZIs used in this state preparation layer and the BPSK transmitter are shown later in Figure 4-4. This configuration is used primarily for stress-testing the system. By using 10 MZIs for the unitary decomposition, as opposed to just three for the binary tree configuration described in the next section, one is subject to error propagation through many more MZIs. In addition, if there are small systematic errors in the

unitary decomposition that lead to a decrease in fidelity - we observed in the previous chapter that the fidelity is not perfect - the channel will be subjected to this error, both in the unitary transmitter and the unitary Green Machine receiver.

4.1.2 Binary tree transmitter

The more robust way to implement the transmitter is with a binary tree MZI structure, shown in the bottom part of the chip in Figure 4-6. In general, implementing an N-mode BPSK transmitter requires (N-1) MZIs with a binary tree, while the unitary decomposition configuration requires $\frac{N(N-1)}{2}$ MZIs.

In the 4-mode transmitter case, by setting the internal phase shifters of all three MZIs in the tree to be $\theta = \pi/2$, one can construct a system of equations to determine the output phases $\{\phi_1, \phi_2, \phi_3\}$ necessary to implement each of the 4 codewords. Here, ϕ_1 corresponds to the external phase shifter of the MZI in the first layer of the tree, and ϕ_2 and ϕ_3 are those of the MZIs in the second layer, from top to bottom.

By illuminating the bottom mode of the MZI in the first layer, MZI #1, we obtain the following simulated phase screen at the output of the chip (up to a global phase):

$$\mathbf{A}_{out} = \begin{bmatrix} 1 \\ e^{i(\pi-\phi_2)} \\ e^{i(\pi-\phi_1-\phi_2+\phi_3)} \\ e^{i(\pi-\phi_1-\phi_2)} \end{bmatrix} \tag{4.2}$$

The required external phases for the (3,4,2) BPSK codeset are shown in Table 4.1 (the top mode is always the same and is considered a reference ancilla). By programming these external phases with internal phases $\theta = \pi/2$ in simulation, we observe a constant intensity front and the desired phase profile we expect to see based on calculations.

While we cannot directly measure the phase front at the output of the transmitter, we measure the output intensity and see that it is fairly constant and only deviates slightly from simulation. This deviation is likely in part due to differences in cou-

	Word 1	Word 2	Word 3	Word 4
ϕ_1	0	0	π	π
ϕ_2	π	0	π	0
ϕ_3	0	π	0	π

Table 4.1: External phase settings for each of three MZIs used to generate each of the four (3,4,2) BPSK codewords.

pling efficiency between different output modes. Experimental normalized intensity is shown in blue in Figure 4-2, while simulated normalized intensity appears in grey.

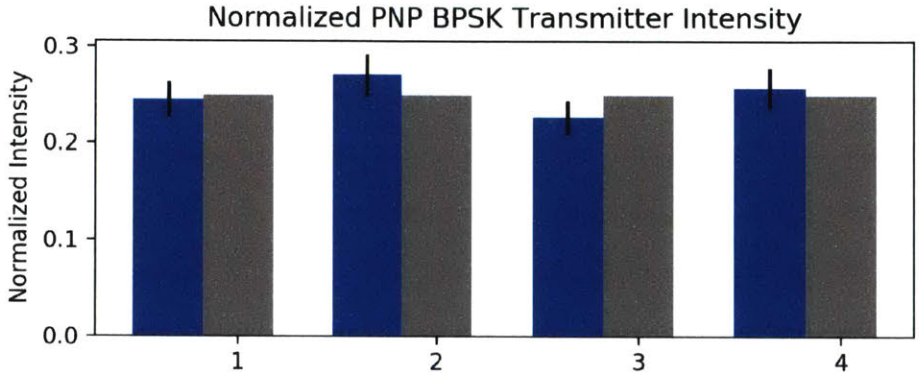

Figure 4-2: Measured (blue) and simulated (grey) output intensity of binary tree BPSK transmitter.

4.2 Joint-Detection Receiver

In theory, an ideal spatial mode channel is represented by the identity operator. Since we can think of the BPSK transmitter as applying a generalized Hadamard transform, $\mathbf{H}_4$, the Green Machine joint detection receiver implements the inverse:

$$\mathbf{U}_{\mathrm{GM}} = \mathbf{H}_4^{-1} = \mathbf{H}_4^{\dagger} = \mathbf{H}_4 \tag{4.3}$$

This is convenient, as one can use the same unitary decomposition to encode the BPSK unitary transmitter and its corresponding Green Machine receiver. We use the same unitary characterization scheme described in the previous chapter to calculate the fidelity of Green Machine generalized Hadamard transform when programmed on

the chip with the Clements [2] decomposition protocol and linear voltage crosstalk correction. Figure 4-3 shows a histogram of the characterized fidelities for 137 instances of programming the Green Machine unitary matrix, both with and without linear voltage crosstalk correction.

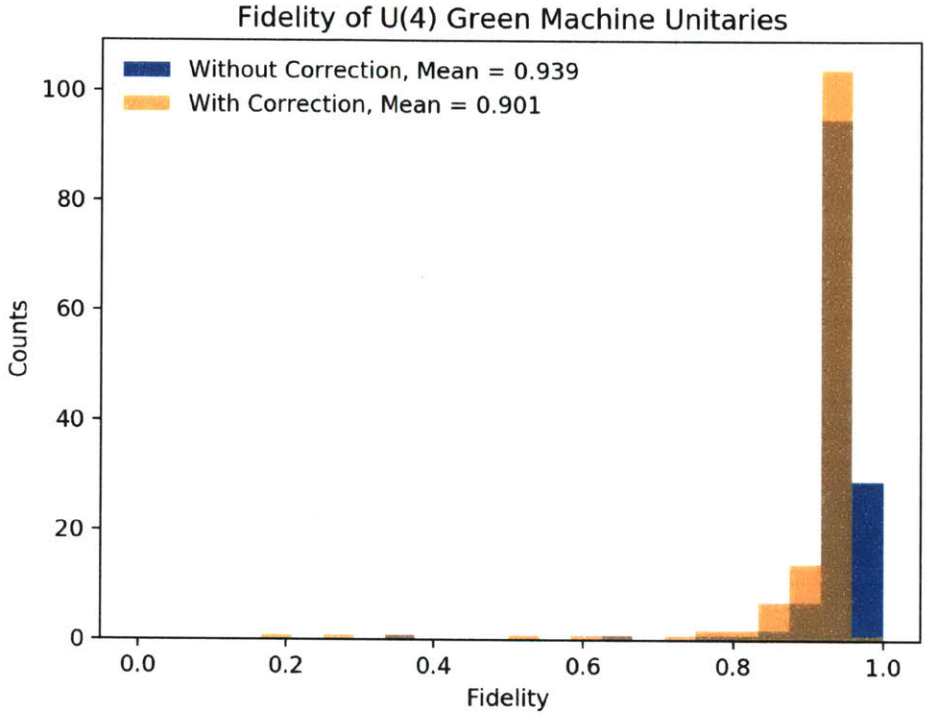

Figure 4-3: Unitary fidelity of U(4) Green Machine receiver circuit, with and without linear voltage crosstalk correction.

We observe a decrease in fidelity after application of crosstalk correction, as well as a wider spread into the low-fidelity range. Further testing is required to see if the polynomial crosstalk model will produce higher fidelities or if using higher input laser power will reduce the noise in the characterization protocol.

4.3 Full Channel

4.3.1 On-Chip Channel

The first demonstration of the PNP BPSK Green Machine (BPSK-GM) channel consists of a state preparation network to select the codeword, a unitary BPSK transmitter, the unitary Green Machine joint-detection receiver, and an output routing identity layer to the photodiode detector array. The entire schematic is shown in Figure 4-4.

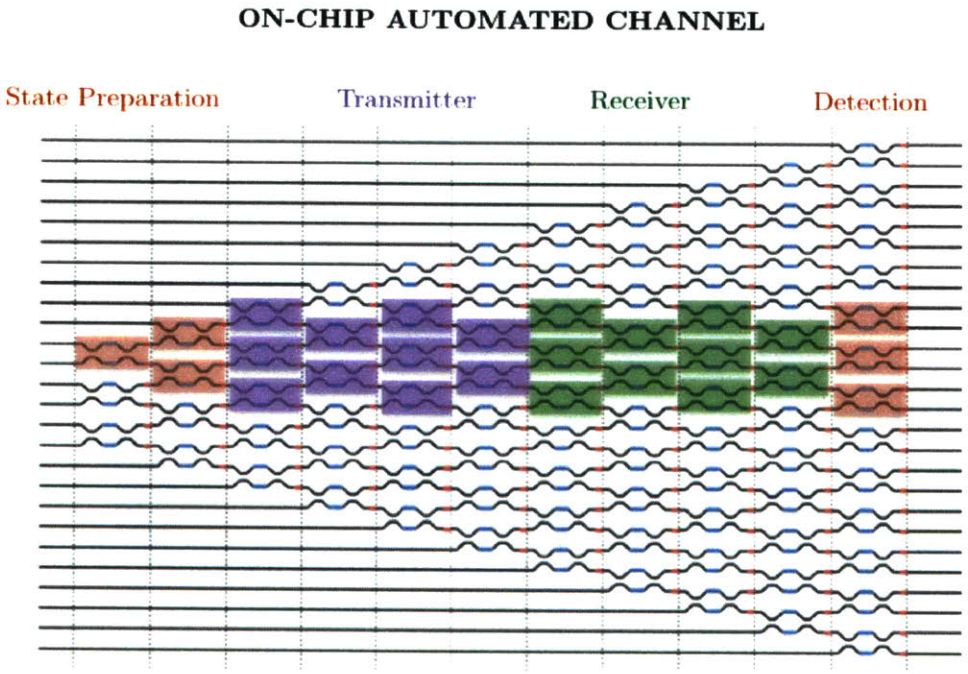

Figure 4-4: PNP circuit layout for BPSK - Green Machine automated channel.

The first step in characterization of the channel is to determine the transition probability matrix, given by the expression in (1.9). Given that Alice sends a particular codeword, x_i, we use strong coherent light and detect the intensity at each output I_j in Bob's receiver to deduce the conditional probabilities:

$$p(y_j|x_i) = \frac{I_j}{\sum_{k=1}^{4} I_k} \tag{4.4}$$

For initial demonstrations with strong light, we do not code over the erasure outcome (due to loss in the channel between Alice and Bob). Figure 4-5 shows the conditional probability matrices, accounting for coupling differences between output modes, for the BPSK-GM channel and an Identity channel, which replaces the transmitter and receiver by N=4 identity matrices.

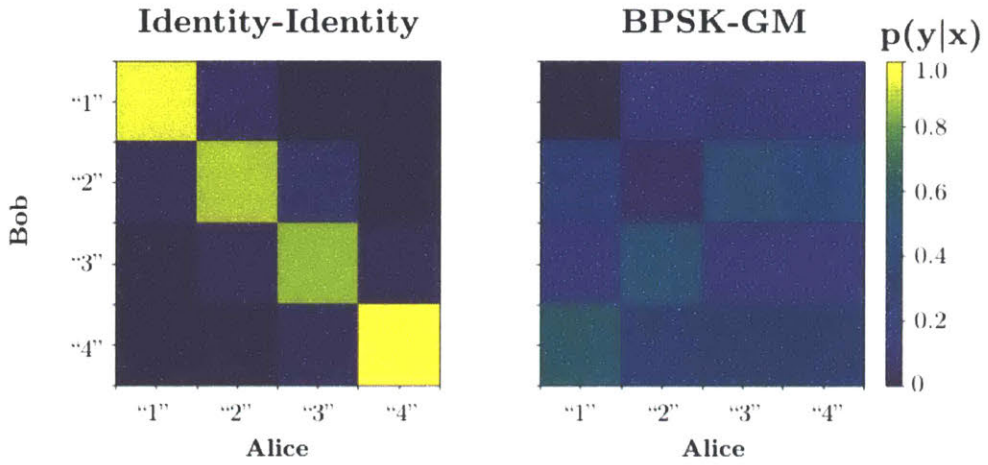

Figure 4-5: Experimentally measured transition probability matrices for the identity transmitter and receiver channel (left) and 4-mode BPSK transmitter and Green Machine receiver (left). Each entry is a conditional probability p(y|x) that, given Alice sent message x, Bob receives message y. We do not yet code over the erasure outcome where Bob does not receive Alice's message.

We observe that there are significant deviations from the ideal identity channel, which should be a diagonal matrix with trace equal to the dimension of the unitary, for the BPSK-GM channel. The identity-identity channel is quite close to the expected result, but some leakage of probability into off-diagonal terms decreases the capacity from the ideal 2 bits to 1.54 bits. This suggests that there must be some programming error introduced by routing and configuring the identity matrices. The deviation from the identity channel in the BPSK-GM was observed in a simulation of the programmed phases as well, indicating that there is error introduced by the unitary decomposition of the GM matrix. When considering an N=2 transform given by a single MZI as an example, we observe that the slope of the output intensity fringe is maximized at the Hadamard setting, $\theta = \pi/2$. Therefore, small deviations in the applied phase lead to the largest errors in output intensity for the Hadamard matrix when compared to all

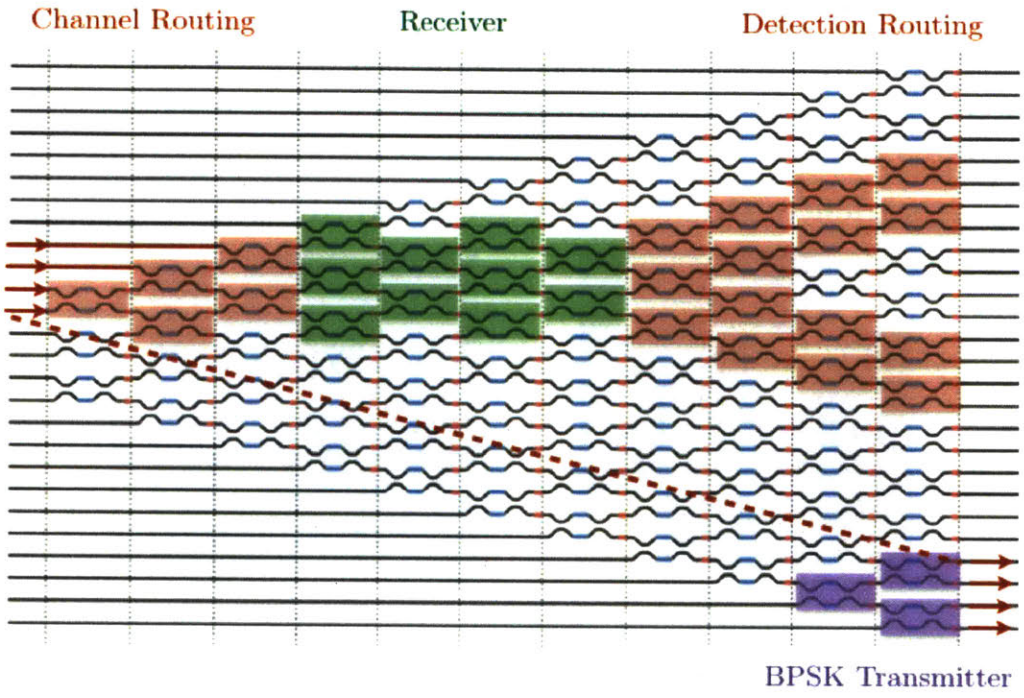

Figure 4-6: PNP circuit layout to simulate chip-to-chip communication between a BPSK binary tree transmitter and a Green Machine 4-mode receiver. Light is input to the BPSK on the first pass through the chip, then the four outputs at the end of the transmitter are wrapped back around to the input of the chip at the receiver section.

other MZI configurations. This is possibly another source of error, but more testing is necessary to deduce whether these errors result primarily from the decomposition, the programming, or both.

4.3.2 Chip-to-Chip Channel

Having obtained a sense of the performance and challenges of the channel under the conditions where the information transfer is occurring in phase-stable integrated waveguides, we then consider the case where the channel connecting Alice and Bob occurs in guided fiber, as would be the case in a fiber-based communication system [32]. In this case, we use the binary tree transmitter to try to minimize all sources

of error, since the fiber-guided channel introduces a phase screen error that was not present in the on-chip channel. A schematic of the configuration is shown in Figure 4-6. The four outputs of the binary tree BPSK transmitter are routed back into the inputs at the top of the chip to the receiver section of the chip. It is important to note that the transmitter must be placed completely out of the light cone (represented by the red dashed line) of the receiver to avoid channel crosstalk. In this configuration, one can emulate chip-to-chip communication with only one chip.

As a first step, we route a wire through both the transmitter section and the receiver section to observe the coupling loss and stability through the channel. We observed an approximately 20dB power loss from the chip input to the chip output. The detector power at the end of the second pass through the chip is shown in Figure 4-7(a). The extinction ratio, measuring the ratio between the power in the desired mode and the next highest mode power, is shown in Figure 4-7(b). The mean extinction ratio over five minutes was 14.1dB. We observe significant power drifts even on the time scale of five minutes, despite insulating the fiber channel with foam. This drop in power is due to coupling drift on the order of minutes.

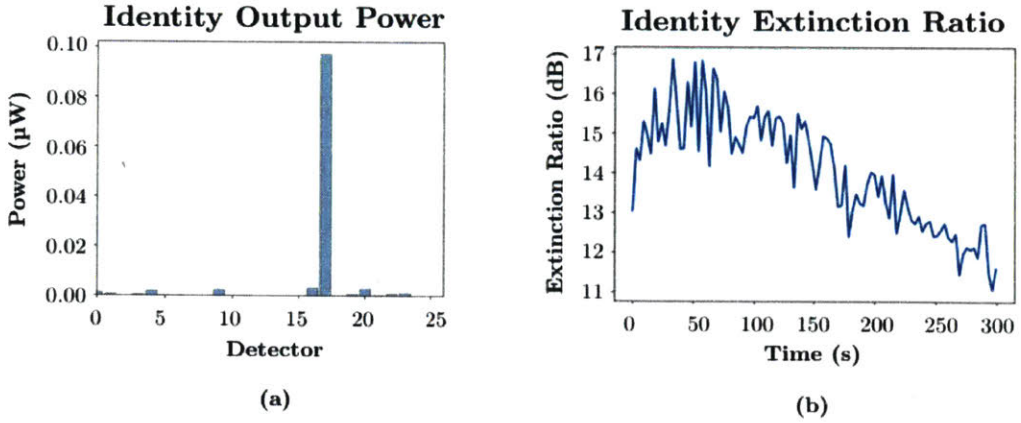

Figure 4-7: (Left) Detector power after two passes through the chip, programmed to identity. (Right) The extinction ratio between the desired output mode and the next highest power leakage mode was measured as a function of time to assess the stability of the chip-to-chip system.

Real-time phase front correction

We determined in the previous subsection that the fiber-guided channel contributes a significant nonideality to the BPSK-GM channel beyond what was considered in the on-chip channel treated in Section 4.3.2. One of the key benefits of using the PNP as a communications system is the capability to dynamically tune its phases, making it robust to many types of dynamic nonidealities. To this end, we implement an algorithm to perform real-time phase front correction of light incident on the receiver after passing through the fiber-guided channel. This would simulate correcting for phase front distortion in a free-space optical channel due to atmospheric turbulence or scintillation [33].

The algorithm takes in a user-defined codeword, indicating which message was sent by Alice. The loss function of the optimization is the sum of the powers on all modes other than the desired output mode corresponding to the given input codeword. The algorithm seeks to minimize the loss function by optimizing over three external phases in the input routing of the receiver section of the chip. Preliminary results of time scans of the real-time optimization on the intensities of each of the four output modes are shown in Figure 4-8.

Each optimization step took between 10 and 15 seconds to complete. Given the short time scale of the fluctuations in the coupling and phase stability of the system and the general coupling drift that independently change the loss function, as demonstrated in Figure 4-7, this is much longer than is acceptable to run the optimization successfully. To combat slow coupling drift, the cost function could be changed to the fractional power in the undesired modes. Fast fluctuations must be further mitigated by improving system stability with improved vibration, temperature, and phase isolation. Additionally, the optimization could be sped up by decreasing averaging on the photodiode readout; however, this would increase the error on the cost function.

One can, in principle, extract the transition probability matrix for this channel from the powers of the four output modes, where each column of the transition matrix is given by a normalized vector of the four measured word intensities. However, we can

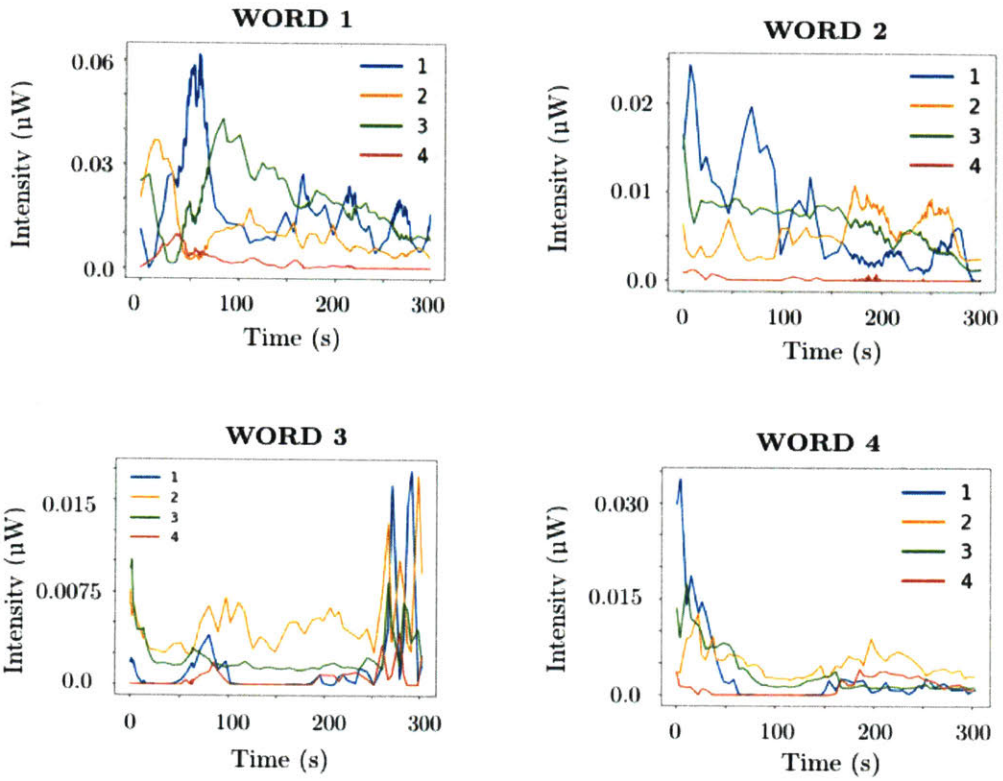

Figure 4-8: Detected intensity of each output mode as a function of time for each of the four BPSK (3,4,2) transmitted codewords, using real-time optimization of receiver input phase screen. Stability of the system prevented the optimization from running successfully and maximizing the power on the output mode corresponding to the transmitted codeword.

see from Figure 4-7 that these intensities vary so quickly and inconsistently compared to each other that calculating the transition matrix for a specific time would be an arbitrary and somewhat meaningless metric upon which to compare the performance of this system to the on-chip channel.

Chapter 5

Discussion and Future Outlook

We have demonstrated a reprogrammable photonic integrated circuit and characterization protocols capable of implementing unitary transforms with high fidelity. The reconfigurability was leveraged to program all aspects of a concatenated code superchannel. The first demonstration takes the form of a stationary channel entirely on chip. The next step implements dynamic phase front correction over a fiber-guided channel, emulating realistic chip-to-chip communication.

Experimental Improvements

We observed significant deviation from the identity transition matrix implemented by an ideal channel. To mitigate these effects, the thermal phase shifter calibration presented in sections 3.2.1 and 3.2.2 will be repeated with the sweeps programmed using the voltage crosstalk corrected values determined according to either the linear or polynomial protocol in section 3.2.4. Additional investigation will also be carried out as to whether the polynomial crosstalk model is more effective in eliminating voltage crosstalk and improving system fidelity.

For these preliminary demonstrations, a 4-spatial-mode channel was chosen. This is due to characterization limitations imposed by the geometry of the MZI configuration on the chip. In particular, to characterize the phases of a unitary transform, all the inputs of the unitary circuit fall within the light cone of at least one input mode. In this case, one would need 12 routing layers to characterize the phases of a U(8)

transformation. However, the current PNP only contains 11 layers, so the maximum unitary size that can be implemented and characterized is U(7). One can, in principle, construct an extra layer to characterize a U(8) unitary transform on the current chip by installing an external beam splitter fed with one input mode and routed at the output to two consecutive chip input modes.

Channel Considerations

For the majority of this thesis, we have been considering a channel consisting of a BPSK transmitter and a Green Machine receiver. However, upon improvements on system stability that enable more effective real-time phase front correction, one can, in principle, tune the phases of the receiver to "learn" the codeset that is being applied at the transmitter. To do this, the real-time optimization will have to use the mutual information as the objective function we seek to maximize over a set of phase knobs. This scheme would implement an optimal receiver for any given unitary transmitter and channel, even if they are varying on a time scale that is longer than the time of the optimization.

In addition, the demonstrations presented in Chapter 4 do not consider the erasure case. With better loss characterization for strong light characterization, eventually running the channel with low mean photon number, $\bar{n}$, and detecting with superconducting nanowire single-photon detectors (SNSPDs), one would have a much more complete set of information about the superchannel. We can then approach Holevo-limited channel capacity and superadditivity of channel capacity in the low photon regime by combining the enhanced superchannel with state-of-the-art turbo codes or Reed-Solomon codes [14, 34].

Bibliography

[1] Michael Reck, Anton Zeilinger, Herbert J. Bernstein, and Philip Bertani. Experimental realization of any discrete unitary operator. 73:58–61, Jul 1994.

[2] William R. Clements, Peter C. Humphreys, Benjamin J. Metcalf, W. Steven Kolthammer, and Ian A. Walmsley. Optimal design for universal multiport interferometers. *Optica*, 3(12):1460–1465, Dec 2016.

[3] G.D. Forney. *Concatenated Codes.* M.I.T. Press research monographs. M.I.T. Press, 1966.

[4] Mrinmoyee Mukherjee. Wireless communication-moving from rf to optical. In *Computing for Sustainable Global Development (INDIACom)*, 2016.

[5] David Thomson, Aaron Zilkie, John E Bowers, Tin Komljenovic, Graham T Reed, Laurent Vivien, Delphine Marris-Morini, Eric Cassan, Léopold Virot, Jean-Marc Fédéli, Jean-Michel Hartmann, Jens H Schmid, Dan-Xia Xu, Frédéric Boeuf, Peter O'Brien, Goran Z Mashanovich, and M Nedeljkovic. Roadmap on silicon photonics. *Journal of Optics*, 18(7):073003, 2016.

[6] Jacob Mower, Nicholas C. Harris, Gregory R. Steinbrecher, Yoav Lahini, and Dirk Englund. High-fidelity quantum state evolution in imperfect photonic integrated circuits. 92:032322, Sep 2015.

[7] Mihika Prabhu Yoav Lahini Jacob Mower Darius Bunandar Changchen Chen Franco N. C. Wong Tom Baehr-Jones Michael Hochberg Seth Lloyd Nicholas C. Harris, Gregory Steinbrecher and Dirk Englund. Quantum transport simulations in a programmable nanophotonic processor. *Nature Photonics*, 11:447–452, June 2017.

[8] Nicholas C. Harris, Yangjin Ma, Jacob Mower, Tom Baehr-Jones, Dirk Englund, Michael Hochberg, and Christophe Galland. Efficient, compact and low loss thermo-optic phase shifter in silicon. *Optics Express*, 22(9), 2014.

[9] Giuseppe Cocorullo, Francesco Della Corte, I Rendina, and M. Sarro Pasqualina. Thermo-optic effect exploitation in silicon microstructures. *Sensors and Actuators A: Physical*, 71(1):19–26, 1998.

[10] Michael R. Watts, Jie Sun, Christopher DeRose, Douglas C. Trotter, Ralph W. Young, and Gregory N. Nielson. Adiabatic thermo-optic mach–zehnder switch. *Opt. Lett.*, 38(5):733–735, Mar 2013.

[11] Chao Qiu, Zhen Sheng, Hao Li, Wei Liu, Le Li, Albert Pang, Aimin Wu, Xi Wang, Shichang Zou, and Fuwan Gan. Fabrication, characterization and loss analysis of silicon nanowaveguides. *J. Lightwave Technol.*, 32(13):2303–2307, Jul 2014.

[12] Thomas M. Cover and Joy A. Thomas. *Elements of Information Theory.* John Wiley and Sons, Inc., 2006.

[13] Daniel J Costello and G David Forney. Channel coding: The road to channel capacity. *Proceedings of the IEEE*, 95(6):1150–1177, 2007.

[14] S. Guha. Structured optical receivers to attain superadditive capacity and the holevo limit. *Physical Review Letters*, 106(24), June 2011.

[15] Zabih Ghassemlooy, Wasiu Popoola, and Sujan Rajbhandari. *Optical Wireless Communications: System and Channel Modelling with MATLAB.* CRC Press, 2017.

[16] B. Menrad and S. Vilevac. Lunar laser communications demonstration: Nasa's first step in developing high-performance laser communications systems, May 2015.

[17] Masahide Sasaki, Kentaro Kato, Masayuki Izutsu, and Osamu Hirota. Quantum channels showing superadditivity in classical capacity. *Phys. Rev. A*, 58:146–158, Jul 1998.

[18] Nicholas C. Harris. *Programmable Nanophotonics for Quantum Information Processing and Artificial Intelligence.* PhD thesis, Massachusetts Institute of Technology, September 2017.

[19] Haijuan Cui, Hongchun Yang, Jun Xu, Zixian Yang, and Yuming Yang. Sublinear current–voltage characteristics of linear photoconductive semiconductor switch. *IEEE Electron Device Letters*, 37(12):1590–1593, 2016.

[20] Steven G. Johnson. Nlopt documentation.

[21] A. H. G. Rinnooy Kan and G. T. Timmer. Stochastic global optimization methods part ii: Multi level methods. *Mathematical Programming*, 39(1):57–78, Sep 1987.

[22] Michael J. D. Powell. The bobyqa algorithm for bound constrained optimization without derivatives. Technical Report NA2009/06, Departmet of Applied Mathematics and Theoretical Physics, Cambridge University, 2009.

[23] M. J. D. Powell. *A Direct Search Optimization Method That Models the Objective and Constraint Functions by Linear Interpolation*, pages 51–67. Springer Netherlands, Dordrecht, 1994.

[24] John A. Nelder and Roger Mead. A simplex method for function minimization. *The Computer Journal*, 7(4):308–313, 1965.

[25] Thomas H. Rowan. *Functional Stability Analysis of Numerical Algorithms.* PhD thesis, University of Texas at Austin, 1990.

[26] Michael A. Nielsen and Isaac L. Chuang. *Quantum Computation and Quantum Information (Cambridge Series on Information and the Natural Sciences).* Cambridge University Press, 1 edition, 01 2004.

[27] Saleh Rahimi-Keshari, Matthew A. Broome, Robert Fickler, Alessandro Fedrizzi, Timothy C. Ralph, and Andrew G. White. Direct characterization of linear-optical networks. *Opt. Express*, 21(11):13450–13458, Jun 2013.

[28] Jacques Carolan. *Universal linear optics: characterization, verification, and computation.* PhD thesis, University of Bristol, 2015.

[29] Fulvio Flamini, Nicolò Spagnolo, Niko Viggianiello, Andrea Crespi, Roberto Osellame, and Fabio Sciarrino. Benchmarking integrated linear-optical architectures for quantum information processing. *Nature Scientific Reports*, 7, 2017.

[30] Mark Lundstrom. *Fundamentals of Carrier Transport.* Cambridge University Press, 2009.

[31] C.T. Kelley. *Iterative Methods for Linear and Nonlinear Equations.* Frontiers in Applied Mathematics. Society for Industrial and Applied Mathematics (SIAM, 3600 Market Street, Floor 6, Philadelphia, PA 19104), 1995.

[32] Eduard Sackinger. *Broadband Circuits for Optical Fiber Communication.* John Wiley and Sons, Inc., 2005.

[33] Kamran Kiasaleh. Performance of apd-based, ppm free-space optical communication systems in atmospheric turbulence. *IEEE Transactions on Communications*, 53(9):1455–1461, Sept 2005.

[34] K. Gracie and M. H. Hamon. Turbo and turbo-like codes: Principles and applications in telecommunications. *Proceedings of the IEEE*, 95(6):1228–1254, June 2007.